Monthly Notices of the ROYAL ASTRONOMICAL SOCIETY

MNRAS **548,** 1–21 (2026)
Advance Access publication 2026 April 9

https://doi.org/10.1093/mnras/stag661

An automated method for planetary nebula detection with SIGNALS: first applications to NGC 4214 and NGC 4449

Nancy Yang [1★] Johanna Hartke [2,3,4] Martin Bureau,[1] Chiara Spiniello,[1,5] Louis-Simon Guité,[6,7] Guy Flint,[1] Magda Arnaboldi,[5] Ana Inés Ennis,[8,9] R. Pierre Martin,[10] Thomas Martin,[11,12] Carmelle Robert,[11] Laurie Rousseau-Nepton,[13,14] Lucas M. Valenzuela [15] and Sébastien Vicens-Mouret[11]

[1]*Sub-department of Astrophysics, Department of Physics, University of Oxford, Denys Wilkinson Building, Keble Road, Oxford OX1 3RH, UK*
[2]*Finnish Centre for Astronomy with ESO (FINCA), University of Turku, FI-20014 Turun yliopisto, Finland*
[3]*Tuorla Observatory, Department of Physics and Astronomy, University of Turku, FI-20014 Turun yliopisto, Finland*
[4]*Turku Collegium for Science, Medicine and Technology (TCSMT), University of Turku, FI-20014 Turun yliopisto, Finland*
[5]*European Southern Observatory, Karl-Schwarzschild-Straße 2, D-85748 Garching bei München, Germany*
[6]*Département d'Astrophysique/AIM CEA/IRFU, CNRS/INSU, Université Paris-Saclay, Université de Paris, F-91191 Gif-sur-Yvette, France*
[7]*Département de Physique, Université de Montréal, Montréal, QC, H3C 3J7, Canada*
[8]*Perimeter Institute for Theoretical Physics, Waterloo, Ontario N2L 2Y5, Canada*
[9]*Waterloo Centre for Astrophysics, University of Waterloo, Waterloo, Ontario N2L 3G1, Canada*
[10]*Department of Physics & Astronomy, University of Hawaii at Hilo, Hilo, 96720, USA*
[11]*Département de Physique, de génie physique et d'optique, Université Laval, G1V 0A6 Québec, Canada*
[12]*Cégep Garneau, 1660 Boulevard de l'Entente, Québec QC G1S 4S3, Canada*
[13]*David A. Dunlap Department of Astronomy and Astrophysics, University of Toronto, 50 St-George Street, Toronto, Ontario M5S 3H4, Canada*
[14]*Dunlap Institute for Astronomy and Astrophysics, 50 St-George Street, Toronto, Ontario M5S 3H4, Canada*
[15]*Universitäts-Sternwarte, Fakultät für Physik, Ludwig-Maximilians-Universität München, Scheinerstr. 1, D-81679 München, Germany*

Accepted 2026 March 30. Received 2026 March 2; in original form 2025 December 23

ABSTRACT

Utilizing the optical imaging Fourier transform spectrograph SITELLE, the Star-formation, Ionized Gas and Nebular Abundances Legacy Survey (SIGNALS) is designed to study the connection between star-forming regions and their environments. Targeting 31 local star-forming galaxies, its data products also lend themselves to planetary nebula (PN) surveys. We present here a new pipeline to find PNe using automated emission-line diagnostics and morphology tests, that is able to distinguish PNe from contaminants with an accuracy similar to that of past visual methods. We also perform thorough completeness tests using mock PNe inserted into the data cubes with full spectra. We apply these tools to a pilot sample of two dwarf irregular galaxies from the SIGNALS survey, NGC 4214 and NGC 4449, with other galaxies to follow. For these two galaxies, we identify 25 PNe (including six new discoveries) and 23 PNe (including 13 new discoveries), respectively, and calculate PN luminosity function distances of $3.09^{+0.25}_{-0.46}$ and $3.91^{+0.33}_{-0.52}$ Mpc, respectively, the latter consistent with previous estimates. We also calculate the bolometric PN specific frequency of our galaxies ($\alpha_{\rm bol}$), as well as a newly defined V-band PN specific frequency ($\alpha_{\rm V}$) based solely on the galaxies' total luminosities in that band.

Key words: surveys – planetary nebulae: general – galaxies: distances and redshifts – galaxies: irregular – galaxies: starburst.

1 INTRODUCTION

Planetary nebula (PNe) are the progeny of low- to intermediate-mass ($\approx$ 1–8 $M_\odot$) stars at the end of their asymptotic giant branch phases (e.g. S. Kwok, C. R. Purton & P. M. Fitzgerald 1978). PNe have varying lifetimes of $\sim$10 000 yr before their ionized shells dissipate. They are almost always brightest in the [O III]λ5007 emission line, although exceptions exist, such as very low-excitation planetary nebulas (PNs) with cool central stars (CSs) that emit more in the Hα line (D. J. Frew & Q. A. Parker 2010). The exact strength of the [O III]λ5007 line depends on the metallicity, initial mass, and temperature of each star, but a high-metallicity PN can emit up to 15 per cent of its CS's luminosity in the [O III]λ5007 line alone (M. A. Dopita, G. H. Jacoby & E. Vassiliadis 1992). The bright [O III]λ5007 emission allows PNs to be detected out to distances of $\approx$100 Mpc (O. Gerhard et al. 2005). PNe can also be detected in galaxy haloes, where the stellar continua are faint. They are therefore popular tools to trace the kinematics of galaxies to large galactocentric radii (e.g. M. Arn-

★ E-mail: nancy.yang@physics.ox.ac.uk

© The Author(s) 2026.
Published by Oxford University Press on behalf of Royal Astronomical Society. This is an Open Access article distributed under the terms of the Creative Commons Attribution License (https://creativecommons.org/licenses/by/4.0/), which permits unrestricted reuse, distribution, and reproduction in any medium, provided the original work is properly cited.

Downloaded from https://academic.oup.com/mnras/article/548/4/stag661/8650714 by Turun kauppakorkeakoulun kirjasto user on 10 June 2026

aboldi et al. 1998; C. Spiniello et al. 2018; J. Hartke et al. 2020; S. Bhattacharya et al. 2023).

PNe also serve as a secondary distance indicator, through the planetary nebulaluminosity function (PNLF). R. Ciardullo et al. (1989) showed that there is a lower limit to the absolute magnitudes of observed PNs (i.e. there is a maximum PN brightness) which is nearly universal across galaxies, regardless of morphological type. By fitting a measured PNLF, this lower limit can be determined and a distance modulus inferred. First described in R. Ciardullo et al. (1989) and adapted for a varying faint-end PNLF slope by A. Longobardi et al. (2013), the PNLF is described by

$$N(M_{5007}) = c_1\, e^{c_2\, M_{5007}} \left(1 - e^{3(M^*_{5007} - M_{5007})}\right) , \quad (1)$$

where M_{5007} is the absolute magnitude of the [O III]λ5007 line, c_1 is a normalization constant, c_2 is the faint-end slope index and M^*_{5007} is the absolute magnitude of the bright-end cut-off. The m_{5007} (apparent) magnitude approximates the V-band (apparent) magnitude one would observe if the total [O III]λ5007 line emission was distributed over the V band, and can be obtained through the integrated [O III]λ5007 flux, F_{5007}, via the Jacoby relation (G. H. Jacoby 1989):

$$m_{5007} = -2.5 \log \left(\frac{F_{5007}}{\mathrm{erg\ s^{-1}\ cm^{-2}}} \right) - 13.74 . \quad (2)$$

PNLF distances can be accurately derived (uncertainties $<$ 10 per cent) for distances of up to ≈20 Mpc (R. Ciardullo 2012; G. H. Jacoby et al. 2024) and have been found to be of comparable precision and accuracy to those derived from Cepheids and tip of the red giant branch (TRGB) methods (see E. Congiu et al. 2025 for a recent comparison).

While the PNLF is effective as a distance indicator, the physics behind the universality of the bright-end cut-off remains unclear. Naively, older stellar populations should have fainter PNs, as older stars exit the main sequence at lower masses and lower progenitor masses produce fainter PNs (P. Marigo et al. 2004). Yet, observations have shown that the bright-end cut-off is always at the same absolute magnitude, so there must be some mechanism(s) for old stellar populations to produce bright PNs (G. H. Jacoby 1989). Recent simulations suggest that these bright PNs may form within older stellar populations of high metallicity, as a result of metal-rich stars (L. M. Valenzuela et al. 2025). Because metal-rich stars evolve more slowly than metal-poor stars of the same mass, they form PNs later and with a higher initial mass, leading to brighter PNs. Metallicity is also predicted to affect the absolute magnitude cut-off, such that M^*_{5007} increases with decreasing metallicities (R. Ciardullo 2010). In turn, one could constrain the metallicity of a galaxy by assuming a distance and fitting for M^*_{5007}.

Another way to investigate stellar populations with PNs is to use the bolometric specific frequency of PNs, that is the number of PNs per unit bolometric luminosity, defined as

$$\alpha \equiv \frac{N_{\mathrm{PN}}}{L_{\mathrm{bol}}} , \quad (3)$$

where N_{PN} is the total number of PNs in a galaxy and L_{bol} is the galaxy's total bolometric luminosity.

In practice, N_{PN} can only be determined over a limited range of magnitudes, down from the bright cut-off. A more practical definition is thus given by

$$\alpha_{\Delta m} = \frac{1}{L_{\mathrm{bol}}} \int_{m^*_{5007}}^{m^*_{5007}+\Delta m} N(m)\mathrm{d}m , \quad (4)$$

where $N(m)$ is the number of PNs between (apparent) magnitudes m and $m + \mathrm{d}m$ and $\Delta m = 2.5$ is commonly used in the literature.

This specific frequency α has long been shown observationally to correlate with galaxy colour (M. Peimbert 1990; R. Ciardullo, G. H. Jacoby & W. E. Harris 1991; R. Ciardullo et al. 2005; A. Buzzoni, M. Arnaboldi & R. L. M. Corradi 2006), such that redder galaxies produce fewer PNs (per unit luminosity). However, stellar population modelling produces the opposite prediction, i.e. redder galaxies should have more PNs (A. Buzzoni et al. 2006).

The specific frequency can also vary as a function of galactocentric radius within a galaxy (X. Hui et al. 1993; A. Longobardi et al. 2013; J. Hartke et al. 2017; S. Bhattacharya et al. 2019).

Traditionally, PN candidates have been identified using the on-band/off-band method, for which follow-up spectroscopy is required to confirm the PN classifications and measure their velocities. Slitless spectroscopy instruments like the Planetary Nebula Spectrograph (N. G. Douglas et al. 2002) offer a more efficient solution, providing PN diagnostics and accurate velocity measurements from a single observation (e.g. L. Coccato et al. 2009; C. Pulsoni et al. 2023).

A further improvement is offered by integral-field spectrographs (IFSs): PNs no longer require dedicated surveys but can be found in IFS data cubes as by-products. Indeed, since the first PN study using IFS (M. Sarzi et al. 2011), there have been many more (e.g. K. Kreckel et al. 2017; F. Scheuermann et al. 2022; but see also the reviews by M. M. Roth et al. 2025 and J. Hartke 2025).

Nevertheless, the effectiveness of most IFSs is limited by their generally small field of views (FOVs), often necessitating numerous pointings for single targets and thus large mosaics (E. Congiu et al. 2025). SITELLE (L. Drissen et al. 2019) is an imaging Fourier transform spectrometer (iFTS) with a very large FOV (11 arcmin × 11 arcmin) mounted at the Canada–France–Hawaii Telescope (CFHT). Its spectral coverage and FOV lend themselves perfectly to PN studies. In particular, the wide FOV allows to study PNs in the outskirts of galaxies, where they stand out easily from the faint stellar continua.

The Star formation, Ionized Gas, and Nebular Abundances Legacy Survey (SIGNALS; L. Rousseau-Nepton et al. 2019) targeted 31 local (distances ≈ 1–12 Mpc) star-forming galaxies with SITELLE. Most past PN surveys have focused on early-type galaxys (ETGs), for their lack of contaminating [O III]-sources (e.g. L. Coccato et al. 2009; A. Cortesi et al. 2013; C. Pulsoni et al. 2018). A PN survey of the SIGNALS galaxies will allow to probe PN population (and associated PNLF) changes with e.g. galaxy morphology (from dwarf irregular galaxies to grand-design spirals), stellar mass and stellar metallicity. So far, the PN populations of only M 31 (T. B. Martin, L. Drissen & A.-L. Melchior 2018) and NGC 4214 (S. Vicens-Mouret et al. 2023) have been catalogued using SIGNALS data. To expand these studies to the entire survey, a more automated pipeline for PN detection is required. This is the primary goal of this work.

This paper thus sets out in detail the automated methods we developed to construct PN catalogues of SIGNALS galaxies. For illustrative purposes, we also applied those methods to the galaxies NGC 4214 and NGC 4449. We describe the data and calibration methods in Section 2. Section 3 covers PN detection, the elimination of contaminants and the construction of mock PN catalogues to estimate the completeness of observations. We present our results for NGC 4214 and NGC 4449 separately in

Downloaded from https://academic.oup.com/mnras/article/548/4/stag661/8650714 by Turun kauppakorkeakoulun kirjasto user on 10 June 2026

Table 1. Overview of targets and observations.

Galaxy	Type	D (Mpc)	Z	Filter	Band (nm)	R	Time/step (s)	Steps	Date
NGC 4214	IAB(s)m	2.93	8.20 ± 0.05	SN2	482–513	943	50	219	2018 May
				SN3	647–685	1895	30	337	2018 May
NGC 4449	IBm	4.01	8.26 ± 0.01	SN2	482–513	943	45.5	219	2020 Feb
				SN3	647–685	4741	13	842	2020 Feb

Note. Columns: (1) Galaxy. (2) Morphological type. (3) Uncertainty-weighted mean distance of a selection of distances from the NASA/IPAC Extragalactic Database. (4) Gas-phase metallicity ($12 + \log(O/H)$) from L. S. Pilyugin, E. K. Grebel & I. A. Zinchenko (2015). (5) SITELLE filter. (6) SITELLE band. (7) Spectral resolution. (8) Integration time per scanning mirror step. (9) Number of scanning mirror steps. (10) Observation date.

Section 4, comparing their PNLF distances and α parameters to those of previous works. We discuss our results in Section 5 and summarize them in Section 6.

Throughout this paper, we refer to [O III]λ5007, [N II]λ6584 and [S II]λλ6716,6731 simply as [O III], [N II], and [S II].

2 DATA AND CALIBRATIONS

2.1 SITELLE

As mentioned above, SITELLE is an iFTS with an 11 arcmin × 11 arcmin FOV (sampled with 0.″32 × 0.″32 spaxels) mounted at the Cassegrain focus of the CFHT (L. Drissen et al. 2019). The design is that of an off-axis Michelson interferometer. A beam splitter directs the light onto two different mirrors: the fixed mirror and the scanning mirror. The two beams meet again at the beam splitter, where they interfere and form two new beams, each recorded with its own camera. The scanning mirror can be moved in small steps, changing the optical path difference between the two beams.

An interferogram cube is obtained by a series of short exposures (≈1 min each), in between which the scanning mirror moves by a few microns. The spectral resolution can be fine-tuned to any resolution in the range 1–10 000 by changing the number of steps of the scanning mirror. A Fourier transform then returns a data cube in which two dimensions are spatial and the third is spectral (wave number). This results in an instrumental line spread function (LSF) that is a sinc as a function of wave number (T. B. Martin, S. Prunet & L. Drissen 2016) rather than the more typical Gaussian as a function of wavelength. Emission (and absorption) lines broadened by the Doppler effect have a Gaussian shape, which when observed with SITELLE is convolved into a 'sincgauss' shape.

Early on during the commissioning of SITELLE, the image quality was found to degrade towards the edges of the FOV, where the point spread function (PSF) becomes elongated. As mentioned in T. B. Martin et al. (2018) and L. Drissen et al. (2019), the extent of this distortion changes from image to image, so it cannot be corrected. Fortunately, however, more recent data suffer less from this issue, thanks to an update to the SITELLE optics (S. Prunet, L. Rousseau-Nepton & M. Baril 2019).

2.2 Data selection

SIGNALS (L. Rousseau-Nepton et al. 2019) is a survey that uses SITELLE's strengths to quantify the impact of environment on star-forming regions, and is therefore optimized to study emission-line objects. SIGNALS uses SITELLE's SN1 (wavelength range 365–385 nm, spectral resolution $R = 1000$), SN2 (480–520 nm, $R = 1000$) and SN3 (651–685 nm, $R = 5000$) filters. It combines large spectral coverage (allowing to observe important emission lines for H II-region and PN studies, such as [O III], H β, H α and [N II]) with high spectral resolution (allowing to measure precise H II-region and PN velocities).

The selection criteria of SIGNALS were driven by the need to observe a large number of H II regions in a variety of galactic environments, resulting in the observations of 31 star-forming galaxies at distances $D \leq 12$ Mpc. While the survey is not optimized to reveal PNs, a previous study by S. Vicens-Mouret et al. (2023) utilized SIGNALS data to identify 15 new PNs in the starburst galaxy NGC 4214. To both illustrate and benchmark our new PN detection pipeline, we thus re-analyse the NGC 4214 SIGNALS data here. Using *Hubble Space Telescope* (*HST*) data, F. Annibali et al. (2017) discovered 28 (potential) PNs in the central region of another similar starburst galaxy, NGC 4449, five of which they obtained full spectra for. We thus also present the SIGNALS data of NGC 4449 here, to add to this catalogue and benchmark our work.

While ≈75 per cent of the stellar populations of NGC 4214 are over ≈8 Gyr old, it is currently undergoing a new burst of star formation (B. F. Williams et al. 2011). NGC 4449 has been continuously forming stars over the lifetime of the galaxy, with a peak of star formation taking place 5–20 Myr ago (E. Sacchi et al. 2018).

We obtained fully calibrated and reduced data cubes from the Canadian Astronomical Data Centre.[1] The SITELLE data reduction pipeline is as described in T. Martin, L. Drissen & G. Joncas (2015), and Table 1 presents an overview of the observations. We assume distances to our galaxies based on listed values from the NASA/IPAC Extragalactic Database [2], using only those derived from primary distance indicators. Where available, distances from the following methods were taken into account: Cepheids, colour–magnitude diagram (CMD), TRGB, and Carbon stars. We only use distances with reported uncertainties.

We note that while SIGNALS uses the SN1 filter, only the data cubes obtained with the SN2 and SN3 filters are used in this work. We also note that while the NGC 4214 data were obtained with a lower spectral resolution in SN3 than the usual SIGNALS' resolution, this does not hinder our ability to detect PNs.

[1] https://www.cadc-ccda.hia-iha.nrc-cnrc.gc.ca/

[2] https://ned.ipac.caltech.edu. The NASA/IPAC Extragalactic Database (NED) is operated by the Jet Propulsion Laboratory, California Institute of Technology, under contract with the National Aeronautics and Space Administration.

Downloaded from https://academic.oup.com/mnras/article/548/4/stag661/8650714 by Turun kauppakorkeakoulun kirjasto user on 10 June 2026

2.3 Flux calibration

While the SIGNALS data cube fluxes are calibrated using standard stars in the aforementioned pipeline, there is still some uncertainty in the zero points. However, we can use narrow-band *HST* data to re-calibrate these zero points (T. B. Martin et al. 2018).

Because for PNs we care most about the [O III] line emission, we focus our calibration on SITELLE's SN2 filter.

We obtained fully calibrated and reduced *HST* images taken in narrow-band filters around [O III], which are fully encompassed by the SN2 filter, from the Barbara A. Mikulski Archive for Space Telescopes.[3] For NGC 4214, we use data taken with *HST*'s Wide Field Camera 3 (WFC3) in the UVIS channel using the F502N filter (programme ID: 11360, PI: R. O'Connell). These data were also used by M. A. Dopita et al. (2010) to identify PN candidates. The WFC3 FOV is 160 arcsec × 160 arcsec, much smaller than SITELLE's FOV, but yielding an overlap area sufficient for calibration (see Fig. 1). For NGC 4449, we use data taken with *HST*'s Advanced Camera for Surveys (ACS) Wide Field Channel (WFC) in a similar F502N filter (programme ID: 10522, PI: D. Calzetti). These data were also used in the PN survey of F. Annibali et al. (2017).

For each galaxy, we integrate the SN2 datacubes over the wave number range of the appropriate F502N filter, scaling each slice by the transmission at that wave number. This simulates an image taken with SITELLE in the F502N filter. We account for the different pixel sizes by re-binning the *HST* images to match the SITELLE pixel size. Finally, we convolve the original *HST* images with a Gaussian to match the seeing of the SITELLE data in the relevant SN2 cube.

We then perform aperture photometry on stars from the *GAIA* Data Release 3 catalogue (Gaia Collaboration 2023) twice, once on the SITELLE slice and once on the re-binned *HST* image. To avoid saturated stars, we select the stars to have apparent *G*-band magnitudes $m_G > 20$, leaving ≈50 stars in the FOV of each galaxy. We extract the fluxes using 8-pixel apertures, subtracting the background flux measured within annuli of radii 10–12 pixels, and compute the ratio of the *HST* and SITELLE fluxes. We then define the correction factor to be the three sigma-clipped median of all the flux ratios. As shown in Fig. 2, the *HST* and SITELLE flux calibrations of NGC 4214 are in very good agreement, but while there is some scatter in the flux ratios of NGC 4449, there is also a clear offset between the two flux calibrations. We assume the uncertainties of our flux calibrations to be the sigma-clipped standard deviations of the flux ratios, and thus recover (re-)calibration factors of 1.00 ± 0.08 and 0.82 ± 0.14 from the *HST* data of NGC 4214 and NGC 4449, respectively. These flux calibrations are optimized for the [O III] line, but we also apply them to other emission lines for consistency. This should not influence the line ratios used in our chosen diagnostic diagrams.

While the galaxies in this paper do have archival *HST* data in the relevant filters, this is not the case for most SIGNALS sample galaxies. Since the survey data products were first released, a more widely applicable flux calibration method has been under development that uses *GAIA* spectra (Gaia Collaboration 2023). This method will be described in detail in an upcoming paper S. Vicens-Mouret et al. (in preparation). For comparison, the new method using *GAIA* spectra yields (preliminary) calibration factors of 0.997 ± 0.032 in SN2 and 0.954 ± 0.024 in SN3 for NGC 4214, and 0.924 ± 0.038 in SN2 and 0.856 ± 0.020 in SN3 for NGC 4449, instead of the ones we derived using *HST* data. The *GAIA*-based flux calibration has the main advantage of being applicable to all SIGNALS galaxies, while only a few galaxies have *HST* data in the relevant filters. In this work we will use the established calibration method using the *HST* data as described here. However, future catalogues will likely be published using the calibrated data from S. Vicens-Mouret et al. (in preparation).

We also correct our line fluxes for Milky Way extinction assuming $R_V = 3.1$, E_{B-V} values taken at the central coordinates of each galaxy from the D. J. Schlegel, D. P. Finkbeiner & M. Davis (1998) dust maps, and a E. L. Fitzpatrick (1999) extinction law.

[3] https://mast.stsci.edu

2.4 Sky-line velocity map

All velocities quoted in this paper have had a barycentric velocity correction applied, based on the start time of the observations.

As described in detail in T. B. Martin et al. (2018), SITELLE's wavelength calibration relies on a high spectral resolution data cube of a laser source, taken with the telescope pointing at the zenith. However, due to temperature variations and the changing direction of the gravity vector, laser cubes obtained for different pointings show (absolute) velocity calibration errors of up to 25 km s^{-1} (N. Flagey et al. 2020). In addition, the exact wavelength of the laser used for the calibration has some uncertainty, as it is dependent on the observing conditions. The data reduction pipeline assumes the manufacturer-stated wavelength of 543.5 nm, but a 0.1 nm error leads to a 55 km s^{-1} offset (T. Martin, L. Drissen & S. Prunet 2021).

To achieve a better accuracy, a fit to the Meinel OH sky lines can be performed in the SN3 filter. Indeed, these should have zero velocity, allowing to map the velocity offset across the SITELLE FOV. As the bright central regions of galaxies do not have clear sky lines, we can not constrain the velocity offsets there by direct fits to the spectra. Nevertheless, we can constrain the velocity offsets at the edges of the FOV and fit a model to those measurements (as a function of position), thus allowing to predict the offset in the central regions. The details of the model and the initial parameters of the fit can be found in T. B. Martin et al. (2018), and they have been implemented in `Outils de Réduction de Cubes Spectraux` (`ORCS`; T. Martin et al. 2015). Here we sampled each cube on a 40 × 40 grid, masking the 5 per cent brightest pixels. The resulting sky velocity maps are presented in Fig. 3. The standard deviation of the residuals from the fit is ≈4 km s^{-1} in both cases, and these have been propagated into our final velocity uncertainties.

The SN2 data cubes do not have any detectable sky line. For PNs which do not have a reliable emission line in SN3, an additional velocity calibration step for the SN2 velocities is presented in Section 3.4.

3 PLANETARY NEBULA PIPELINE

The construction of our PN catalogues can be broken down into two main steps: (i) finding PN candidates and (ii) distinguishing PNs from contaminants. In this section, we describe these two steps in detail. We start with the creation of a two-dimensional (2D) image from which we detect emission-line sources. The emission lines are then fitted and diagnostic diagrams are used to weed out H II regions and supernova remnants (SNRs). Finally,

Downloaded from https://academic.oup.com/mnras/article/548/4/stag661/8650714 by Turun kauppakorkeakoulun kirjasto user on 10 June 2026

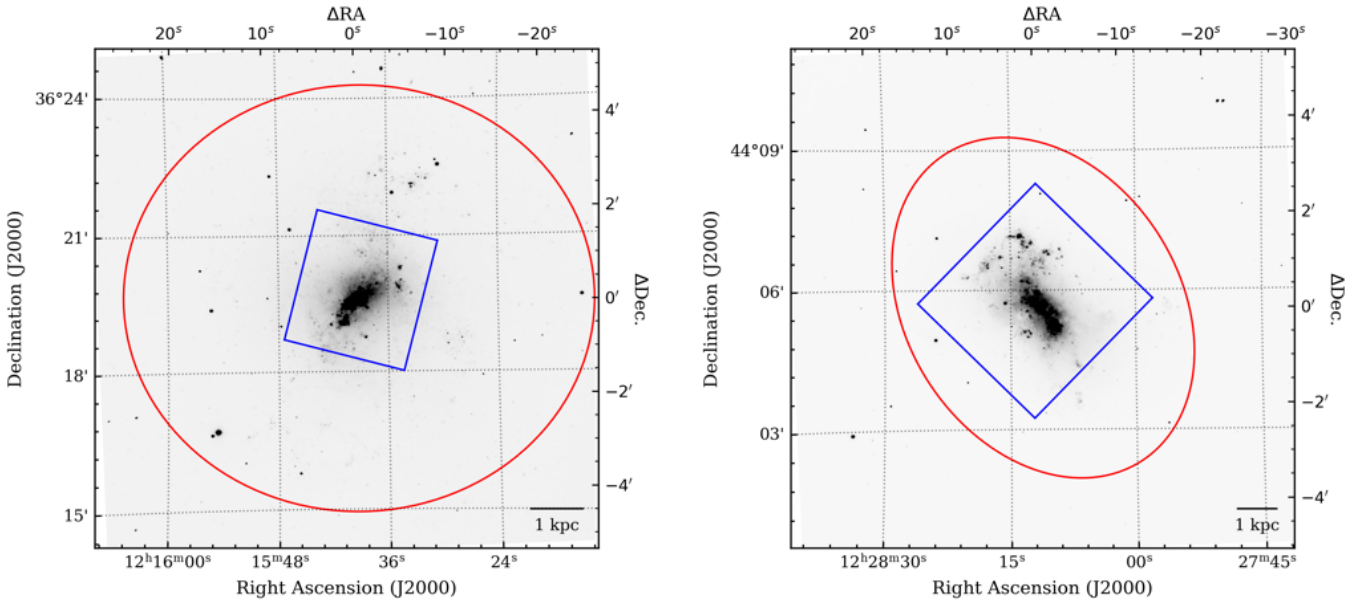

(a) NGC 4214 (b) NGC 4449

Figure 1. SITELLE SN2 deep images of NGC 4214 (left) and NGC 4449 (right). Rectangles are overlaid to indicate the FOVs of the corresponding *HST* images, taken with WFC3 (left) and ACS (right). The ellipses represent the apertures used by D. O. Cook et al. (2014), whose total B and V magnitudes we adopt.

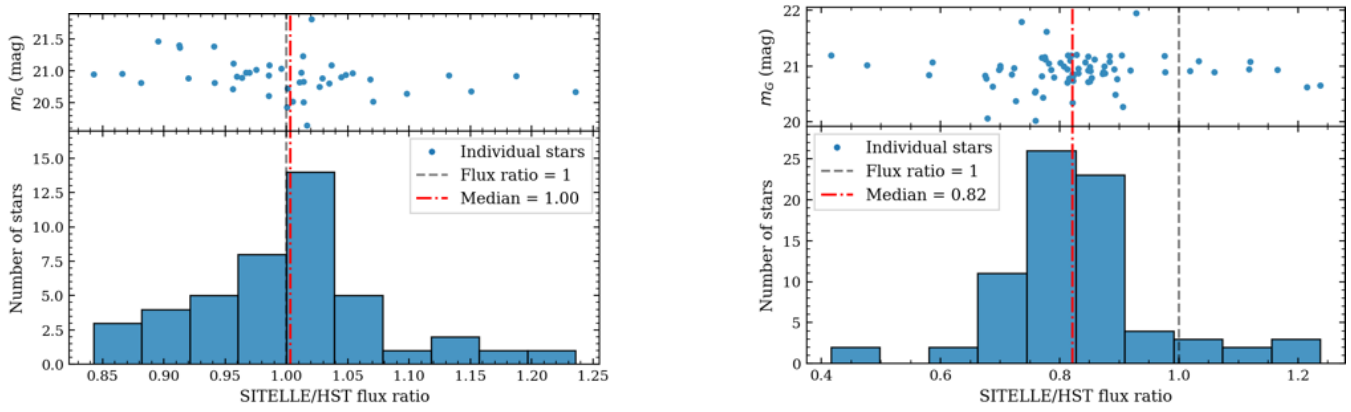

(a) NGC 4214 (b) NGC 4449

Figure 2. Flux correction factors of NGC 4214 (bottom-left) and NGC 4449 (bottom-right), determined by taking the flux ratios of stars measured using the SITELLE SN2 data cube (integrated over a narrowband *HST* filter) and an *HST* image. The sigma-clipped medians are indicated by red dot-dashed vertical lines, ratios of 1 by grey dashed vertical lines. The apparent *GAIA G*-band magnitudes of the stars used are shown in the top parts of the plots.

we remove sources whose morphologies are inconsistent with a point-source. See Fig. 4 for an overview of our PN detection pipeline, including map-making and calibration steps.

3.1 Source identification

To identify emission-line objects, we created a so-called detection map using an inbuilt function of ORCS (T. Martin et al. 2015), as used in T. B. Martin et al. (2018). The process is similar to median filtering. At each spaxel, the median spectrum of a $9 \times 9\,\mathrm{pixel}^2$ 'background' spatial box (excluding the central $3 \times 3\,\mathrm{pixel}^2$) is first subtracted from the median spectrum of a $3 \times 3\,\mathrm{pixel}^2$ spatial box, both centred on the spaxel under consideration. The highest flux at any wave number of this background-subtracted spectrum is then assigned to the spaxel. This procedure therefore reveals sources that are brighter than their surroundings in at least one (wave-number) frame. By applying this procedures to our SN2 data cubes, we highlight sources that are bright in either [O III]λ5007, [O III]λ4959 or H β. The box sizes quoted here are the default options, chosen to fit the typical seeing of SITELLE observations (≈1 arcsec or ≈3 pixels). While the sizes can be changed, they are restricted to odd numbers of pixels and therefore cannot be precisely fine-tuned.

We search for objects in the SN2 detection map using the DAOFIND algorithm (P. B. Stetson 1987) as implemented in PYTHON by L. Bradley et al. (2022). This finds local maxima with peak fluxes above a certain threshold flux. The routine `DAOStarFinder` also returns two different roundness measures for each detected source, but we opted not to use those in the

Downloaded from https://academic.oup.com/mnras/article/548/4/stag661/8650714 by Turun kauppakorkeakoulun kirjasto user on 10 June 2026

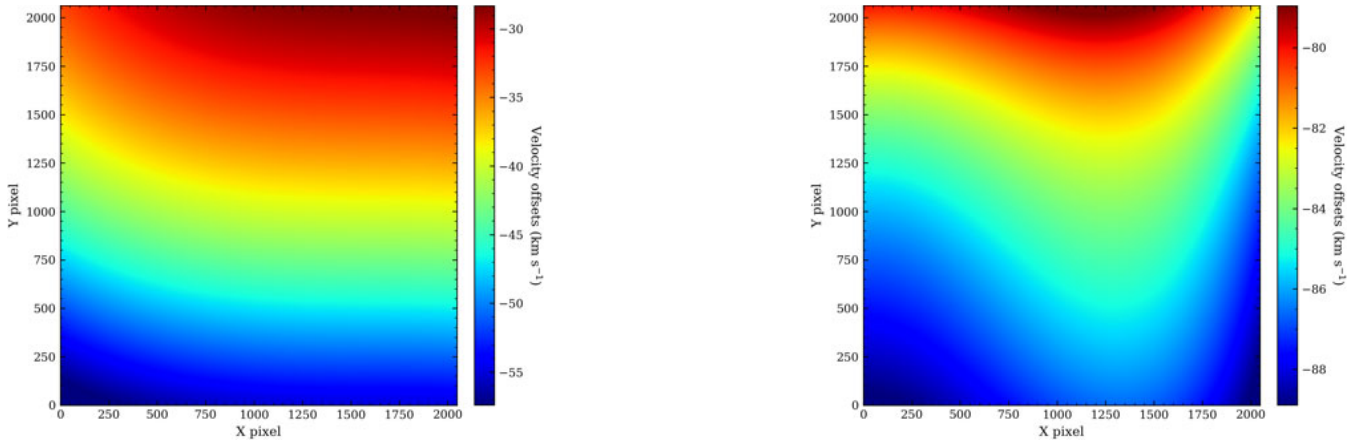

(a) NGC 4214 (b) NGC 4449

Figure 3. Fitted map of velocity offsets across the SITELLE FOV, as measured from sky lines in the SN3 filter, for NGC 4214 (left) and NGC 4449 (right). The images cover the same FOV and have the same orientations as those in Fig. 1.

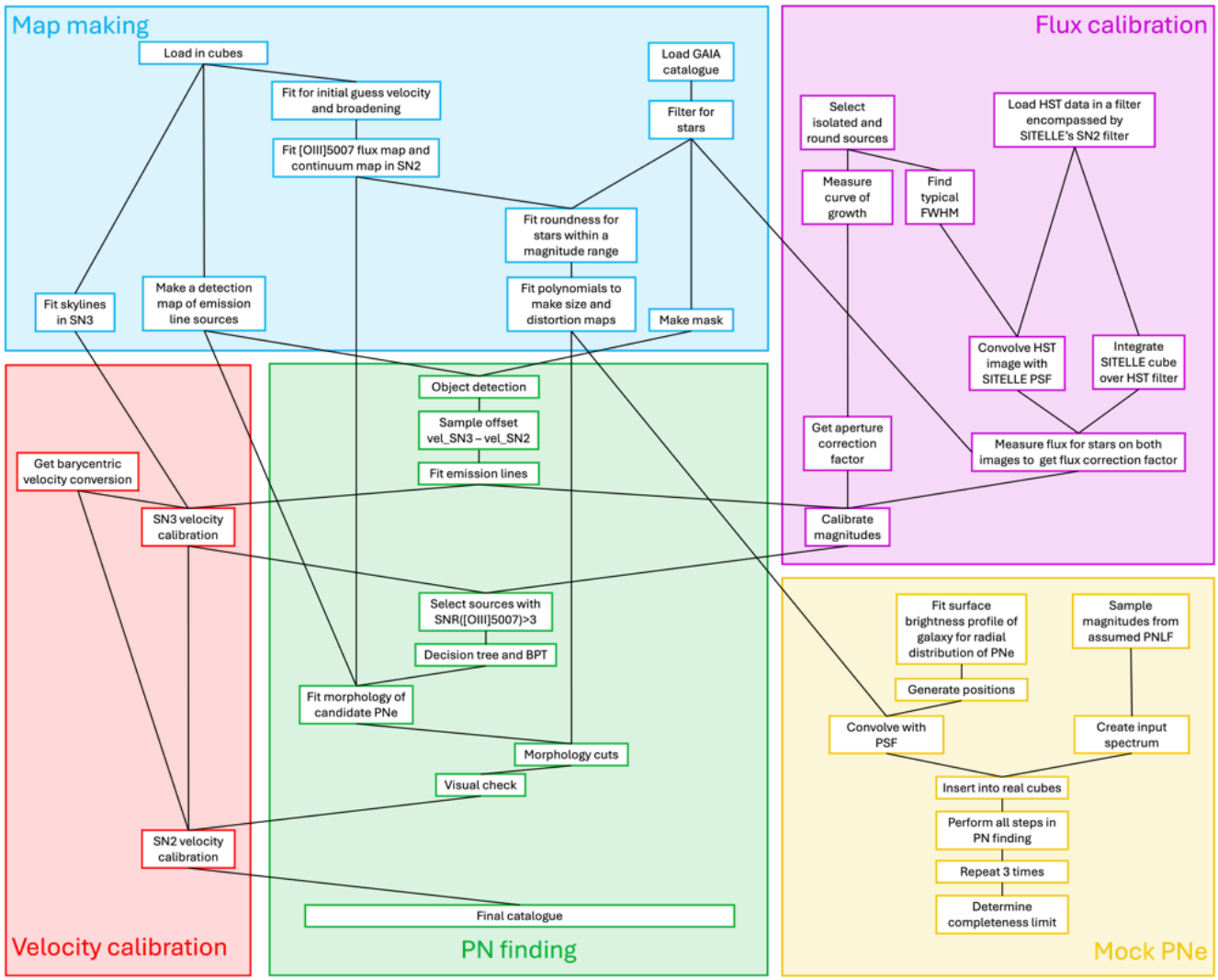

Figure 4. Schematic illustration of the SIGNALS PN identification pipeline.

Downloaded from https://academic.oup.com/mnras/article/548/4/stag661/8650714 by Turun kauppakorkeakoulun kirjasto user on 10 June 2026

following steps as both measures turned out to be correlated with magnitude. We therefore proceed with the source centroids only, and (re-)fit their roundnesses later.

Running the algorithm on the detection maps yields ≈5000 sources for each galaxy. Most of these sources are associated with H II regions, but using the detection map is nevertheless preferable to using a simple map of the [O III]λ5007 emission, as H II regions are very bright and extended in [O III]. The detection map is better at revealing point sources, which is extremely useful when searching for PNe; any source bright and compact in [O III] should also be prominent in the detection map. To illustrate this, we show a comparison of (part of) the deep image (constructed by integrating over all frames of the interference data cube before Fourier transforming), the [O III] map and the detection map of NGC 4449 in Fig. 5.

3.2 Source spectra and photometry

We use ORCS (T. Martin et al. 2015) for emission-line fitting, which relies on the `curve_fit` function of the SCIPY library (P. Virtanen et al. 2020). For each emission-line source identified in the detection map, we extract a spectrum from a circular aperture of 3 pixels in radius, from which we subtract the median spectrum from a background annulus of inner radius 8 and outer radius 10 pixels. The typical full width at half maximum (FWHM) is ≈3 pixels, but we purposefully keep the aperture small to minimize contamination from other sources (A. A. Soemitro et al. 2023). This is the same aperture used by S. Vicens-Mouret et al. (2023) and increases the signal-to-noise ratio (S/N; S. B. Howell 1989). The small aperture does introduce the need for an aperture correction, which we determine by constructing the curves of growth of round, isolated sources. As the PSFs of the SN2 and SN3 data cubes are different, we measure this correction separately for each data cube. For NGC 4214, the aperture correction factors used are 1.35 ± 0.11 for SN2 and 1.34 ± 0.12 for SN3. For NGC 4449, they are 1.35 ± 0.19 for SN2 and 1.40 ± 0.20 for SN3.

When fitting emission lines, ORCS has the option to fit the velocity and velocity dispersion of each line separately. We did not use this option, however, as we assume PN emission lines are from a single source (superpositions are unlikely in these low-mass galaxies). This has the added benefit of yielding more robust velocity measurements, as all the lines can be used simultaneously to determine a single velocity and velocity dispersion.

Good initial guesses of the velocities of the sources are required for the fits to be accurate. To illustrate this, we generated mock PN spectra with varying background noise. We set the spectral resolution to match that of the datacubes of NGC 4449, which is the SIGNALS standard. We then fitted these spectra with a range of initial velocity guesses, to test the limits within which the fits still converge to the correct velocity. We show the results in Fig. 6. For SN2, the fitting procedure yields the correct velocity as long as the initial guess is within ≈300 km s^{-1} of the truth, which is a wider range than the velocity dispersion of the galaxies studied. For SN3, the allowed range is smaller and an initial guess within ≈100 km s^{-1} of the truth is required. This is due to the SN3 cube having a higher spectral resolution, which is SIGNALS standard practice. In contrast to the strong dependence on spectral resolution, there is only a small dependence on signal-to-noise ratio.

For the galaxies in this paper, we select a suitable initial velocity guess by fitting the emission lines of the 30 brightest sources identified using `DAOStarFinder`. These fits are checked by eye to ensure a good fit to the appropriate lines and yield: (1) an initial guess for the velocity and (2) a typical offset of the fitted velocities $\Delta v = v_{\rm SN3} - v_{\rm SN2}$. The two galaxies in this paper do not have a large velocity gradient, so we assume that the PNs will also have velocities within 300 km s^{-1} of the sampled velocity. Under this assumption, the initial velocity guess should allow lines in the SN2 filter to be fitted correctly for all our candidate PNs. The resulting $v_{\rm SN2}$ can then be used as the initial guess for the emission lines in the SN3 filter, by applying Δv. To account for the uncertainty in $v_{\rm SN2}$ and to allow for some variation of Δv, we also re-fit SN3 with initial velocities 100 km s^{-1} above and below the initial guess of $\Delta v + v_{\rm SN2}$. From these, we select the best fit based on the reduced χ^2. While for these galaxies we performed three SN3 fits per source, this number can be increased as necessary to allow for a greater range of velocities.

After fitting, we apply an [O III] luminosity cut, keeping only sources with a reliable [O III] detection, defined as an [O III] flux S/N $>$ 3. As PNs are generally brightest in the [O III] emission line, we would risk eliminating many PNs by requiring a similarly strong detection of any other emission line. We thus define other emission lines as reliably detected if they have flux S/N $>$ 1, and adopt 1σ flux upper limits for non-detections.

3.3 Contaminant elimination

3.3.1 Emission-line ratio diagnostics

The next step is to distinguish PNs from other emission-line sources. The most common contaminants are H II regions and SNRs, although background intermediate-redshift galaxies are also occasionally detected in [O III]. While PNs can have emission-line ratios very similar to those of some of these contaminants (D. J. Frew & Q. A. Parker 2010), in most cases only they occupy a specific area in the top-left corner of a typical emission-line ratio diagnostic diagram (so-called BPT diagrams; J. A. Baldwin, M. M. Phillips & R. Terlevich 1981).

We use the demarcation line of G. Kauffmann et al. (2003) on the [N II]-BPT and L. J. Kewley et al. (2001) on the [S II]-BPT to filter out H II regions. The empirical L. Sabin et al. (2013) demarcation line is used on both diagrams to filter out SNRs. As many of our sources are undetected in one or more emission lines, we have allowed for and evaluated every combination of detections and non-detections in a decision tree, shown in Fig. A1.

For most candidates, both the [N II]-BPT and [S II]-BPT diagrams will be considered in some form. The use of two diagnostic diagrams means that we have two intermediate classifications that may not always match, and that need to be consolidated into one final conclusion. To avoid confusion, we only discuss the intermediate classifications in this section and consolidate the results in Section 3.3.3.

Fig. 7 shows the BPT diagrams for the emission-line sources of both galaxies, with colours indicating the intermediate classifications. Let us consider the case of a source with all emission lines detected. Sources located within the PN-only region are considered likely PN candidates. These are indicated by blue symbols in Fig. 7. If a source could be located within the PN-only region when considering its emission-line ratio uncertainties, it is then considered a possible PN candidate. These are indicated by green symbols in Fig. 7. A source not satisfying either criterion is rejected as not a PN (i.e. a contaminant, plotted in grey in Fig. 7).

Also plotted in Fig. 7, but using triangles, are sources with emission-line flux upper limits. For these, we consider whether

Downloaded from https://academic.oup.com/mnras/article/548/4/stag661/8650714 by Turun kauppakorkeakoulun kirjasto user on 10 June 2026

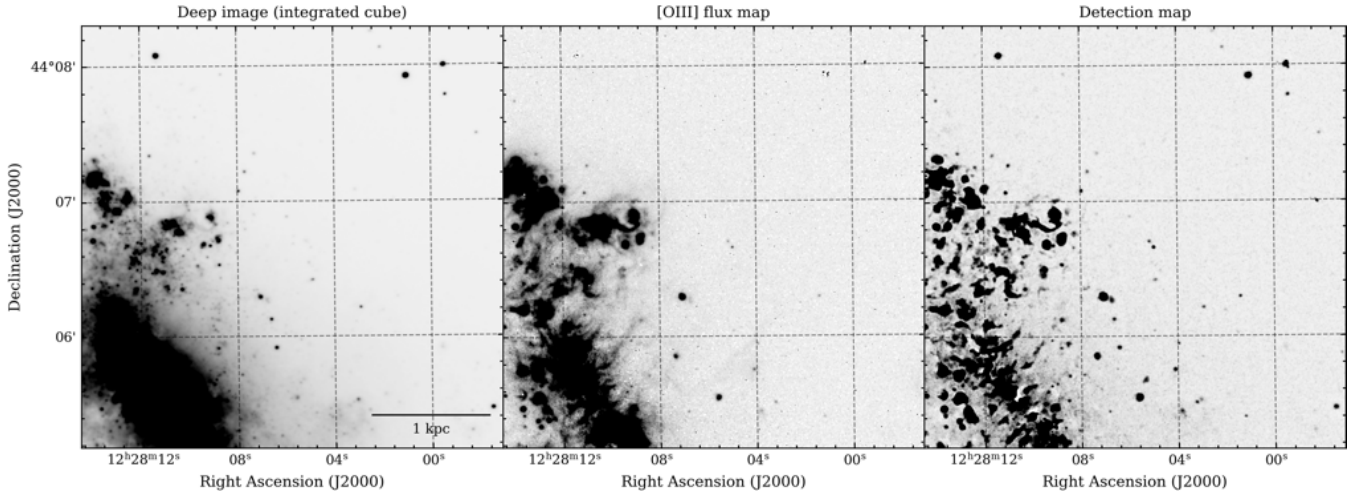

Figure 5. Inner section of the deep image (left), [O III] map (centre) and detection map (right) of NGC 4449. The single black pixels in the central panel show spaxels for which the emission-line fit failed. As expected, these are more common toward the edge of the map.

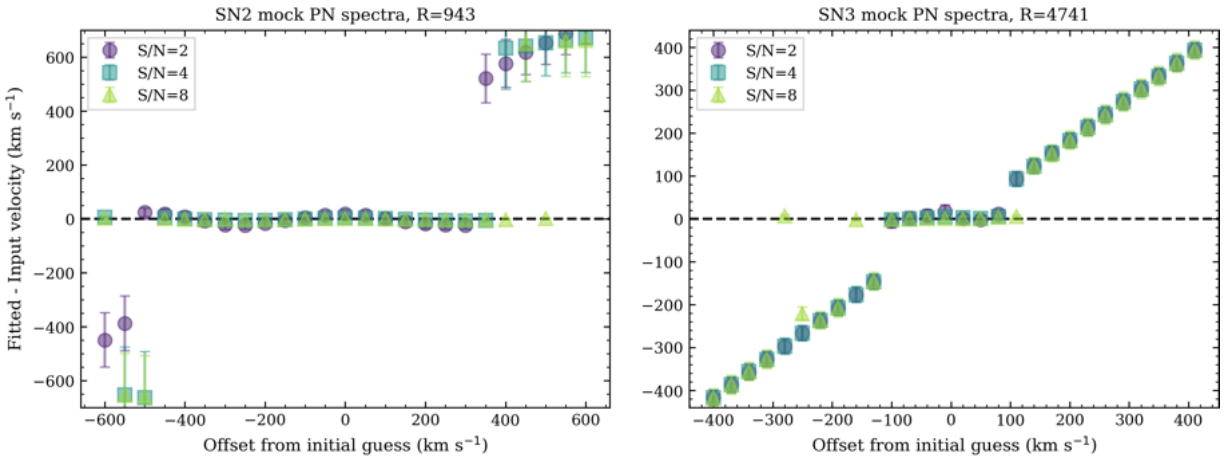

Figure 6. Fitting accuracy of mock spectra as a function of initial velocity guess and signal-to-noise ratio.

the direction of the limit makes a source point away from, or toward, the PN-only region. In doing so, we consider the demarcation lines (and the regions they delineate) to be defined only as far as the emission-line flux ratio ranges plotted in Fig. 7. For example, the PN-only region does not extend to infinity above the L. Sabin et al. (2013) line. The intermediate classifications of sources with upper limits are illustrated in Fig. 8 for the [N II]-BPT; they are analogous for the [S II]-BPT.

A direct consequence of our classification criteria, as indicated in the decision tree (Fig. A1), is that we classify an emission-line source as a possible PN if it has a reliable [O III] detection but no other emission-line detection. This will almost always be the case for the faintest PNs detectable. As a consequence, we can only ever label these as possible PNs, rather than likely PNs.

Another special case is an emission-line source with reliable [O III] and [N II] detections but no other emission-line detection, as this is characteristic of Type I PNs (M. Peimbert & S. Torres-Peimbert 1983; S. Torres-Peimbert & M. Peimbert 1997). For these objects, we first consider their position on the [N II]-BPT as usual. If they are not in the PN-only region, we still classify them as possible PNs if they have $\log([\mathrm{N\,II}]/[\mathrm{O\,III}]) \geq -0.3$. For the galaxies presented in this paper, there is no Type I PN.

3.3.2 *Source morphology*

Spatially unresolved objects like PNs should be spatially identical to the PSF, and should therefore appear as circular Gaussian-shaped objects. As H II regions and SNRs are usually spatially extended, the extents and shapes of emission-line sources are of great help to remove potential contaminants remaining after applying the aforementioned emission-line ratio diagnostics. However, the SITELLE PSF varies across the FOV, objects being more distorted toward the edges. A point source located far from the data cube centre could therefore appear more extended and elongated, making it more difficult to distinguish it from an intrinsically extended source. We have therefore attempted to map the PSF variations across the FOV, so that we can still apply compactness and shape criteria to determine whether a PN candidate (based on emission-line ratios) is indeed a spatially unresolved PN.

We map the variations of the PSF in SN2 by quantifying the departures from perfect 2D Gaussians of sources across the FOV.

Downloaded from https://academic.oup.com/mnras/article/548/4/stag661/8650714 by Turun kauppakorkeakoulun kirjasto user on 10 June 2026

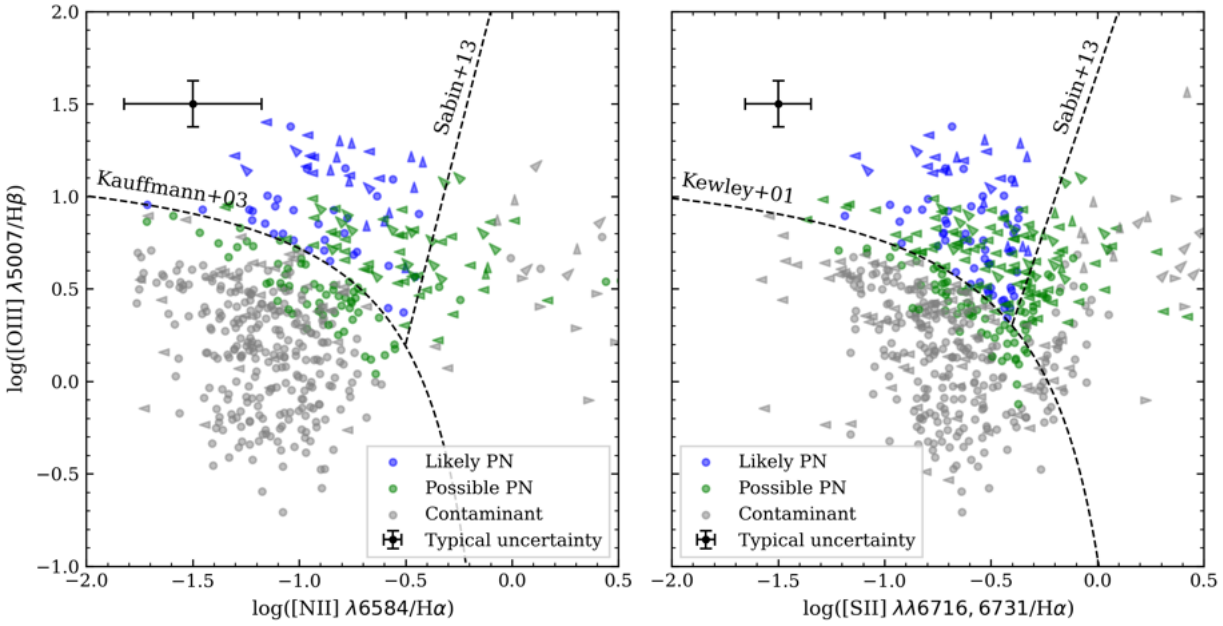

(a) NGC 4214

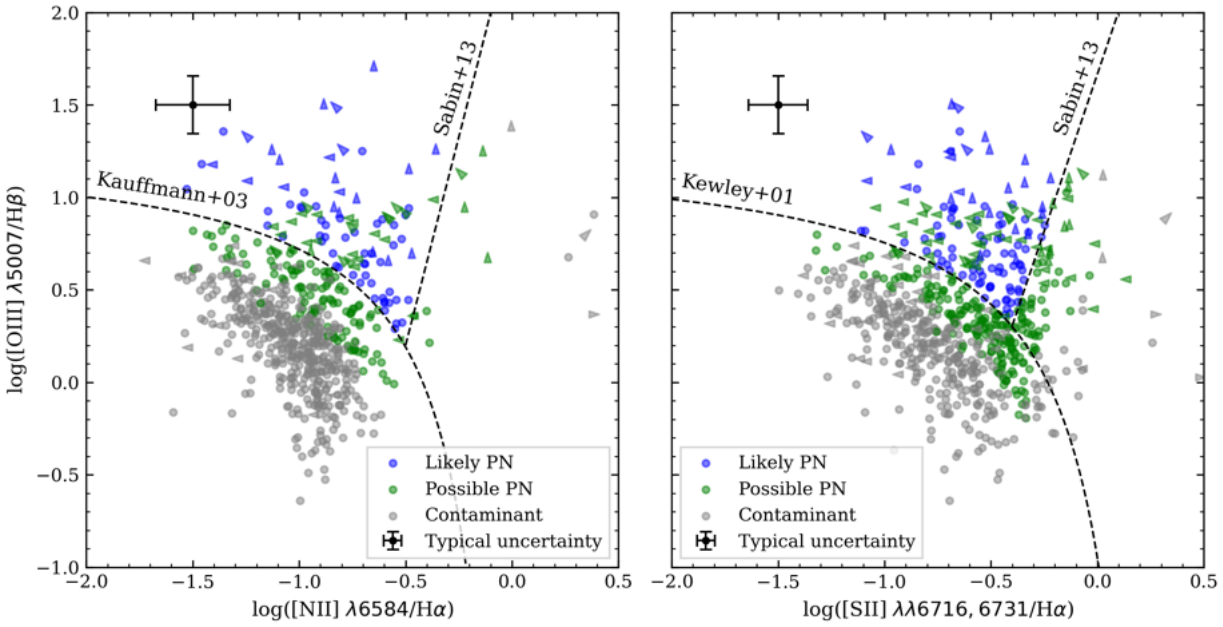

(b) NGC 4449

Figure 7. Classification of the emission-line sources of NGC 4214 (top) and NGC 4449 (bottom), based on the [N II]-BPT diagram (left) and the [S II]-BPT diagram (right). Triangular markers indicate limits and their directions, in cases of non-detection of at least one of the emission lines.

We use all the stars from the *GAIA* Data Release 3 (Gaia Collaboration 2023) catalogue that are located within the SITELLE FOV and have $m_G > 17$ (to avoid saturated stars). We filter for stars using `classprob_dsc_combmod_star` > 0.995, which indicates the probability of any source being a single star.

We then fit the stars' shapes on the SN2 continuum map using 2D Gaussians, and define a distortion parameter $\mathcal{D} \equiv 1 - \frac{\sigma_b}{\sigma_a}$, where σ is the standard deviation of the best-fitting Gaussian and a and b refer to the best-fitting Gaussian major and minor axis, respectively. A perfectly round source has $\mathcal{D} = 0$ while an elongated source has $0 < \mathcal{D} < 1$. We then fit a polynomial surface to all the measurements across the FOV, yielding the 2D distortion map ($\mathcal{D}_{\rm fit}$) shown in Fig. 9 for each of NGC 4214 and NGC 4449. Each map informs us on how elongated an intrinsically round source appears in our data.

Having fitted the *GAIA* stars, we then carry out 2D Gaussian fits of all the [O III] emission-line sources. The S/N of PNs in the deep images are not sufficient to carry out reliable fits, as they are only emitting across a very limited number of frames in each data cube. We therefore fit the emission-line sources using the [O III] flux maps and the detection maps, and calculate a distortion parameter $\mathcal{D}_{\rm source}$ from each map. Each can then be

Downloaded from https://academic.oup.com/mnras/article/548/4/stag661/8650714 by Turun kauppakorkeakoulun kirjasto user on 10 June 2026

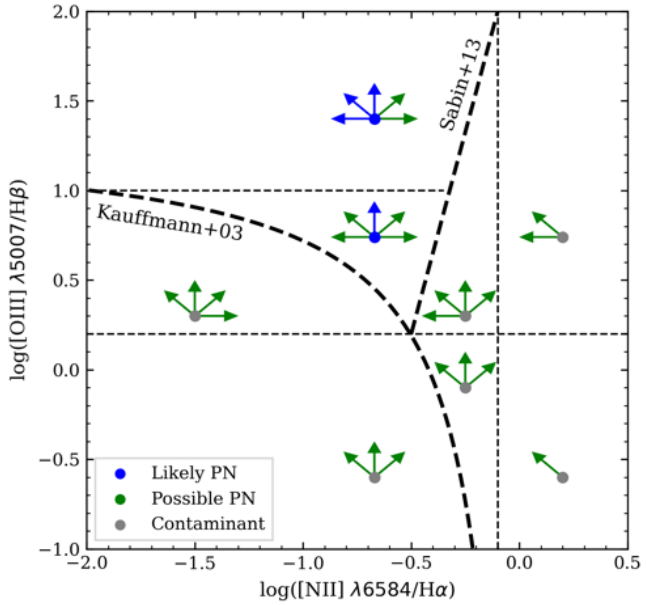

Figure 8. [N II]-BPT diagnostic diagram, illustrating how a source is classified based on its location and emission-line ratio lower/upper limits. Diagonally pointing arrows indicate an upper limit along two axes. The horizontal line at $\log([O\,\mathrm{III}]/\mathrm{H}\,\beta) = 0.2$ shows the intersection of the G. Kauffmann et al. (2003) and L. Sabin et al. (2013) demarcation lines. The horizontal line at $\log([O\,\mathrm{III}]/\mathrm{H}\,\beta) = 1$ and the vertical line at $\log([N\,\mathrm{II}]/\mathrm{H}\,\alpha) = -0.1$ are there because we only consider the demarcation lines as far as the boundaries plotted here. There is no down-pointing arrow as we require each emission-line source to have a reliable [O III] detection.

compared to the prediction of the polynomial fit at the source location. We classify sources as round if $\mathcal{D}_{\mathrm{source}} - \mathcal{D}_{\mathrm{fit}} \leq 0.3$ for at least one of the two maps.

PNs should also be spatially unresolved. We thus fit another polynomial surface, this time simply to the semimajor axes (σ_{a}) of the stars (see Fig. 10). We classify a PN candidate as unresolved if $\sigma_{\mathrm{a,source}}/\sigma_{\mathrm{a,fit}} \leq 1.3$.

3.3.3 *Final catalogue*

We visually inspect all the sources that are (1) round, unresolved and classified as a likely PN on at least one of the two BPT diagrams, and (2) round, unresolved and classified as a possible PN on both diagnostic diagrams (or on the only one used). Objects from category (1) that pass the visual inspection are labelled bona fide PNs, while those from category (2) are labelled possible PNs. The final classifications of all objects that are at least possible PNs are shown in Tables B1 and B2 for NGC 4214 and NGC 4449, respectively.

3.4 Velocity calibration

While the SN3 initial velocities were based on the uncalibrated SN2 velocities (Section 3.2), the resulting fitted SN3 velocities are usually of a higher precision and can be calibrated using the skyline method described in Section 2.4. The exceptions to this are sources that have S/N $<$ 3 in the H α line, for which the SN2-based velocities generally remain more reliable. Nevertheless, the SN2 filter has a much lower spectral resolution and, more importantly, it lacks (detected) sky lines required for a velocity calibration. We thus calibrate the SN2 velocities of these PNs by finding the average offset between the uncalibrated SN2 velocities and the fully calibrated SN3 velocities of nearby objects. This method is very similar to that used by S. Vicens-Mouret et al. (2023), but we nevertheless explain it in full here as a few modifications were made.

First, we compile a catalogue of sources that are reliably detected (flux S/N $>$ 3) in both [O III] and H α, so that these sources have velocities estimated using both the SN2 (v_{SN2}) and the SN3 (v_{SN3}) filters. These sources are not required to have PN-like emission or be point sources. As we can use the skyline calibration for SN3, we treat the calibrated SN3 velocities as the ground truths. For each PN that does not have a velocity derived using the SN3 filter, we search for objects within a radius of 150 pixels, iteratively increasing that radius by 100 pixels at a time, if necessary, until at least 20 sources are found. We then calculate the median $v_{\mathrm{SN3}} - v_{\mathrm{SN2}}$ of these sources, and use that as a correction factor for the PN SN2 velocity. For error propagation, the standard deviation of all the $v_{\mathrm{SN3}} - v_{\mathrm{SN2}}$ measurements is taken as the uncertainty of the correction factor.

This method assumes that the extra correction to the SN2-derived velocities varies smoothly across the FOV, but we can test its accuracy by also applying it to sources which do have SN3 (sky line-based) velocities. The outcome of this is shown in Fig. 11 for NGC 4449, revealing that the corrected SN2 and SN3 velocities of the sources follow the 1 : 1 line, with a standard deviation of $\approx$20 km s^{-1}. The velocities of sources detected only in SN2 may therefore be slightly less reliable. In this work, we quote the SN3 velocities for sources with S/N $>$ 3 in the H α line, SN2 velocities otherwise.

3.5 Mock catalogue and recovery tests

To better understand our recovery rate and to define a completeness limit for our PN catalogues, we generate mock populations of PNs. As PNs are the progeny of stars, their distribution should to first order reflect that of the underlying stellar light. We therefore start by performing surface photometry of each galaxy, and use that to dictate where the mock PNs are inserted spatially. We first mask out sources identified as stars by *GAIA*, as these do not belong to the galaxy. To avoid being biased by emission-line regions, we use a map of the galaxy (stellar) continuum emission in SN2. We then carry out surface photometry, fitting the surface brightness in elliptical annuli of constant ellipticity, position angle and centre. We use 12 annuli, increasing the semimajor and semiminor axes logarithmically. The relative surface brightness of each annulus determines the number of mock PNs it receives. Within each elliptical annulus, the positions of the mock PNs are randomized. To test the PN recovery as a function of apparent magnitude, we also randomly sample the magnitudes from an assumed Ciardullo-like PNLF (R. Ciardullo et al. 1989). In doing so, we need to assume a bright-end cut-off and therefore a distance to each galaxy, but this does not affect the completeness limit inferred, which is at a much fainter magnitude. The distance used for each galaxy is as listed in Table 1.

To insert each PN in a data cube, we create a 2D Gaussian spatial model using ASTROPY , with input parameters as determined from foreground stars. For each mock PN, we take the fitted σ_{a} and $\mathcal{D}$ at its input position, using the maps created in Section 3.3.2.

The spectra of the mock PNs are scaled versions of each other, in the sense that the [O III] flux matches that of the sampled m_{5007}.

Downloaded from https://academic.oup.com/mnras/article/548/4/stag661/8650714 by Turun kauppakorkeakoulun kirjasto user on 10 June 2026

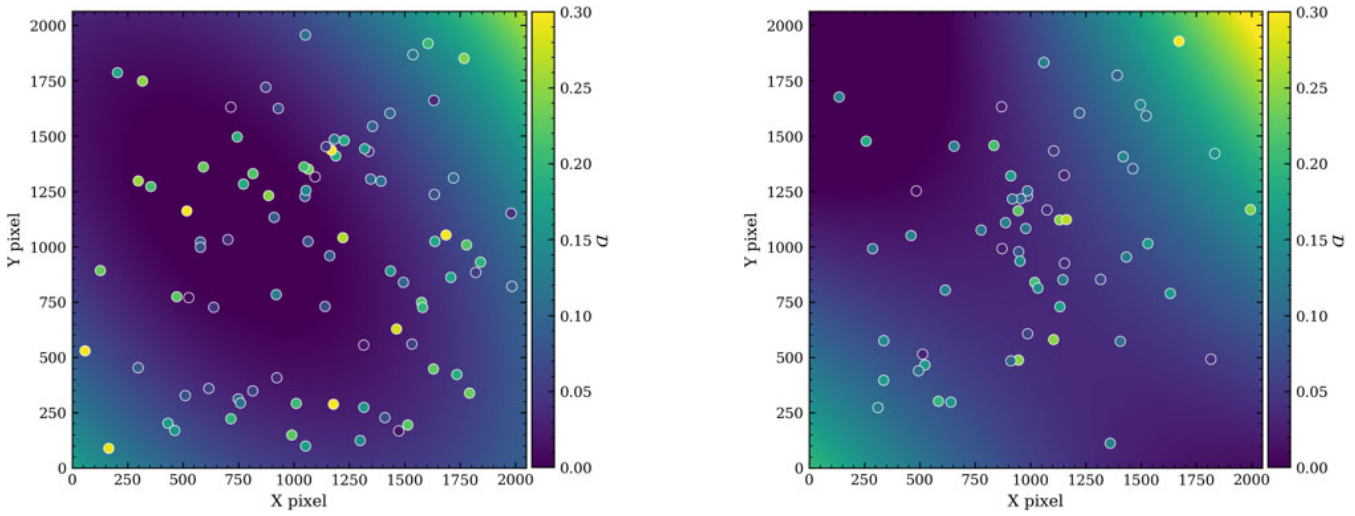

(a) NGC 4214 (b) NGC 4449

Figure 9. Distortion maps of NGC 4214 (left) and NGC 4449 (right), fitted to stars. The stars used for the fit are plotted as filled circles, with a colour matching that of the background map and colour table. Lighter colours indicate higher asymmetric distortions.

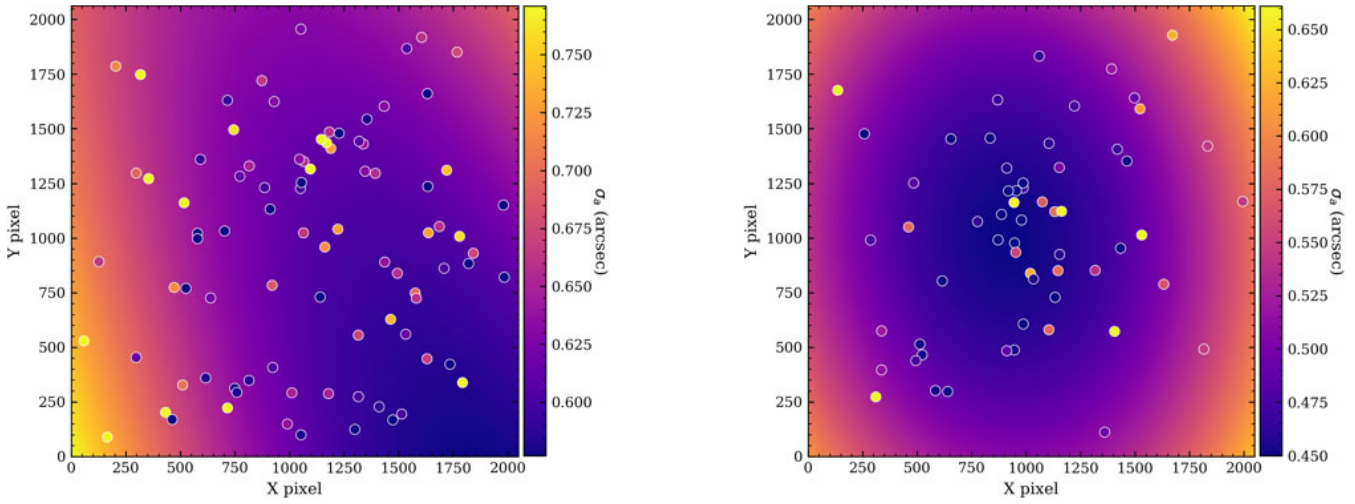

(a) NGC 4214 (b) NGC 4449

Figure 10. σ_a maps of NGC 4214 (left) and NGC 4449 (right), fitted to stars. The stars used for the fit are plotted as filled circles, with a colour matching that of the background map and colour table. Lighter colours indicate larger σ_a and therefore more severe size distortions.

We select input emission-line ratios, such that a source with these emission lines would be located in the appropriate region of each BPT diagram, and assign the same ratios to each mock PN. ORCS is then used to simulate SN2 and SN3 spectra at spectral resolutions matching that of the real data cubes, assuming the same velocity offsets and broadening as the real PNs.

Finally, the mock PNs are inserted into the real data cubes, to best recreate the conditions under which real PNs are searched for (e.g. same noise and contaminant sources). To ensure sufficient numbers of mock PNs (and thus reliable statistics) but avoid source confusion, for each galaxy we create three unique sets of mock data cubes with ≈300 PNs in each.

Using the same methods as for the real catalogue, we create a detection map using ORCS , run our source detection algorithms using `photutils` and carry out emission-line fitting with the same parameters as for the real data. We then cross-match the input mock PNs with the recovered sources. Fig. 12 shows how our mock PNs populate the [N II]-BPT emission-line ratio diagnostic diagram, where the input emission-line ratios are indicated by the red star. The colour coding of the data points shows that the scatter of the mock PNs about the input emission-line ratios increases with faintness (larger magnitudes) and proximity to the galaxy centre (increased contamination due to bright H II regions).

The mock PN roundnesses were determined from the mock detection frames and the mock [O III] flux maps using only the automated method (no visual inspection). We use the same distortion maps and size maps as fitted before ($\mathcal{D}_{\rm fit}$ and $\sigma_{\rm a}$) to determine whether sources are sufficiently round. We also keep the size cuts the same. The total recovery rates and corresponding PNLFs are shown in the left panels of Fig. 13. We consider the samples complete in magnitude bins for which the recovery rate is at least 50 per cent. This yields completeness limits of $m_{5007} = 25.5$ for NGC 4214 and $m_{5007} = 24.7$ for NGC 4449.

Downloaded from https://academic.oup.com/mnras/article/548/4/stag661/8650714 by Turun kauppakorkeakoulun kirjasto user on 10 June 2026

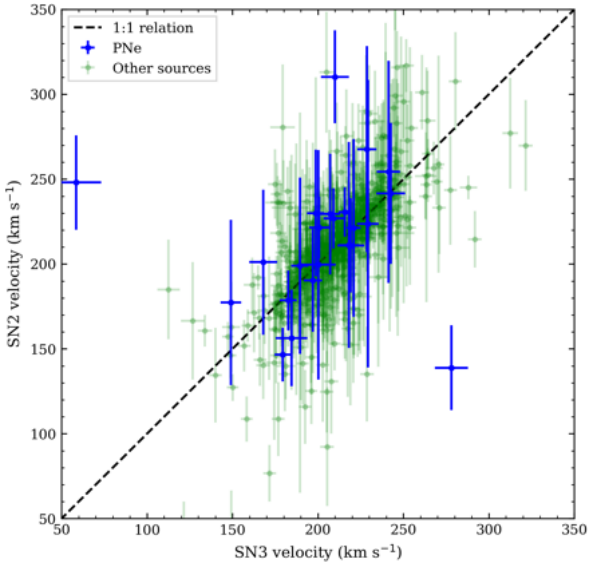

Figure 11. Comparison of the SN2 (cross-matching) and SN3 (sky-line) velocity calibration methods for sources in NGC 4449.

The strong dependence on magnitude present in the left panels of Fig. 13 is expected, but we can also investigate the spatial dependences of the completeness of our samples by considering only the subsets of mock PNs brighter than the completeness limits. As illustrated in the right panels of Fig. 13, the recovery rates are low in the galaxy centres, due to the bright and extended contaminant emission-line regions there. By having the mock PN positions follow the stellar continuum light, many are indeed located in the galaxy central regions where they are harder to detect. If we had populated the data cubes randomly spatially, we would have significantly overestimated the completeness of our samples.

3.6 PNLF and the α parameter

The planetary nebulae luminosity function specifies the number of PNs within a certain m_{5007} range. It has empirically been shown to function as a distance indicator through its bright-end cut-off, applicable to both early- and late-type galaxies. It is described by equation (1), but we use the simplified version that keeps the faint-end slope index fixed at $c_2 = 0.307$ and we assume an absolute magnitude of the bright-end cut-off $M^*_{5007} = -4.47$ (R. Ciardullo 2012). The only parameter we fit for is the apparent magnitude of the bright-end cut-off (m^*_{5007}), for which we use the method of maximum likelihood (R. Ciardullo et al. 1989) as implemented by F. Scheuermann et al. (2022). By treating the PNLF as a probability distribution, we avoid binning the PNs in magnitude. For the initial guess of the distance modulus we assume the distance listed in Table 1 for each galaxy, which is the mean of the distances listed in the NASA/IPAC Extragalactic Data base. For NGC 4214 and NGC 4449, these come from a combination of methods including TRGB.

The specific frequency of PNs, also referred to as the α parameter, is defined in equations (3) and (4). Although α is traditionally defined using a bolometric luminosity, it has become common practice to use B or V band photometry with a bolometric correction, as described in A. Buzzoni et al. (2006). We also follow this convention and calculate $\alpha_{\rm bol}$ parameters based on V-band photometry from D. O. Cook et al. (2014), using the integrated magnitudes obtained from their infrared apertures as they most closely match the areas over which we detect PNs (see Fig. 1). We assume distances as listed in Table. 1, rather than the ones derived from PNLF fitting. In addition to $\alpha_{\rm bol}$, we provide an α_V parameter for each galaxy, which simply uses the V-band luminosity without a bolometric correction.

The number of PNs we recover is only a subset of the entire population of PNs, even at bright magnitudes. This needs to be accounted for when calculating the α parameter. For each galaxy, we determine the recovery rate using the mock catalogue of PNs. This recovery rate as a function of magnitude is then used to scale the number of recovered PNs to what should be more representative of the full population. To facilitate comparisons between surveys of varying depth, the α parameter is often defined up to 0.5 or 2.5 mag from m^*_{5007}. It should be noted that with a completeness threshold defined at 50 per cent, the PN catalogue of NGC 4449 is only complete up to 0.5 mag from the fitted bright-end cut-off.

4 RESULTS

4.1 NGC 4214

In NGC 4214, we identify 628 sources with reliably detected [O III] emission. Of these, 279 (potentially) have emission-line ratios in the appropriate regions of the BPT diagnostic diagrams and 121 are initially classified as round using our automated methods. The 72 sources that are in both of those categories were then visually inspected for roundness, leaving only 11 bona fide and 14 possible PNs. Most of the final contaminants that were manually removed fall within the bright centre of the galaxy, where we cannot make out whether the source is a distinct point source or not. Other contaminants are associated with extended sources, where it is unclear if they are part of the larger source or superposed. We have kept our catalogue as clean as possible and removed any source that does not appear to be a point source.

The final PN catalogue of NGC 4214 is presented in Table B1. The PN spatial distribution is shown in the left panel of Fig. 14. There is a notable lack of PN in the brightest part of the galaxy, as expected from the mock PN recovery test (Fig. 13).

Of the 17 PN candidates identified by M. A. Dopita et al. (2010) using narrow-band *HST* imaging, we do not recover D9–D12 and D16 on the detection map. It should however be noted that M. A. Dopita et al. (2010) suspected D10 and D13 to be compact high-excitation H II regions rather than PNs. All the other candidates that are detected also have strong enough [O III] emission. D13 and D15 do not have the right emission line ratios, while D2 and D8 are rejected because of their morphologies. In the end, we classify six of the 17 M. A. Dopita et al. (2010) PN candidates as bona fide PNs and a further two as possible PNs. Our conclusions are very similar to those of S. Vicens-Mouret et al. (2023), who recovered the same 8 PNs but also included D2 and D15 in their catalogue.

All of the 25 PNs identified with the SIGNALS data by eye by S. Vicens-Mouret et al. (2023), including the 10 that are in common with M. A. Dopita et al. (2010), are also recovered on the detection map. However, VDR1 and VDR10 are not reliably detected in the [O III] emission line (S/N $\leq$ 3), while VDR4 and VDR14 are not in the appropriate region of either BPT diagnostic diagram. Aside from these four mentioned here, and D2 and D15 mentioned before, we we stil classify 10 of the 25 S. Vicens-Mouret et al. (2023) PNs as bona fide PNs and a further nine as possible PNs.

Downloaded from https://academic.oup.com/mnras/article/548/4/stag661/8650714 by Turun kauppakorkeakoulun kirjasto user on 10 June 2026

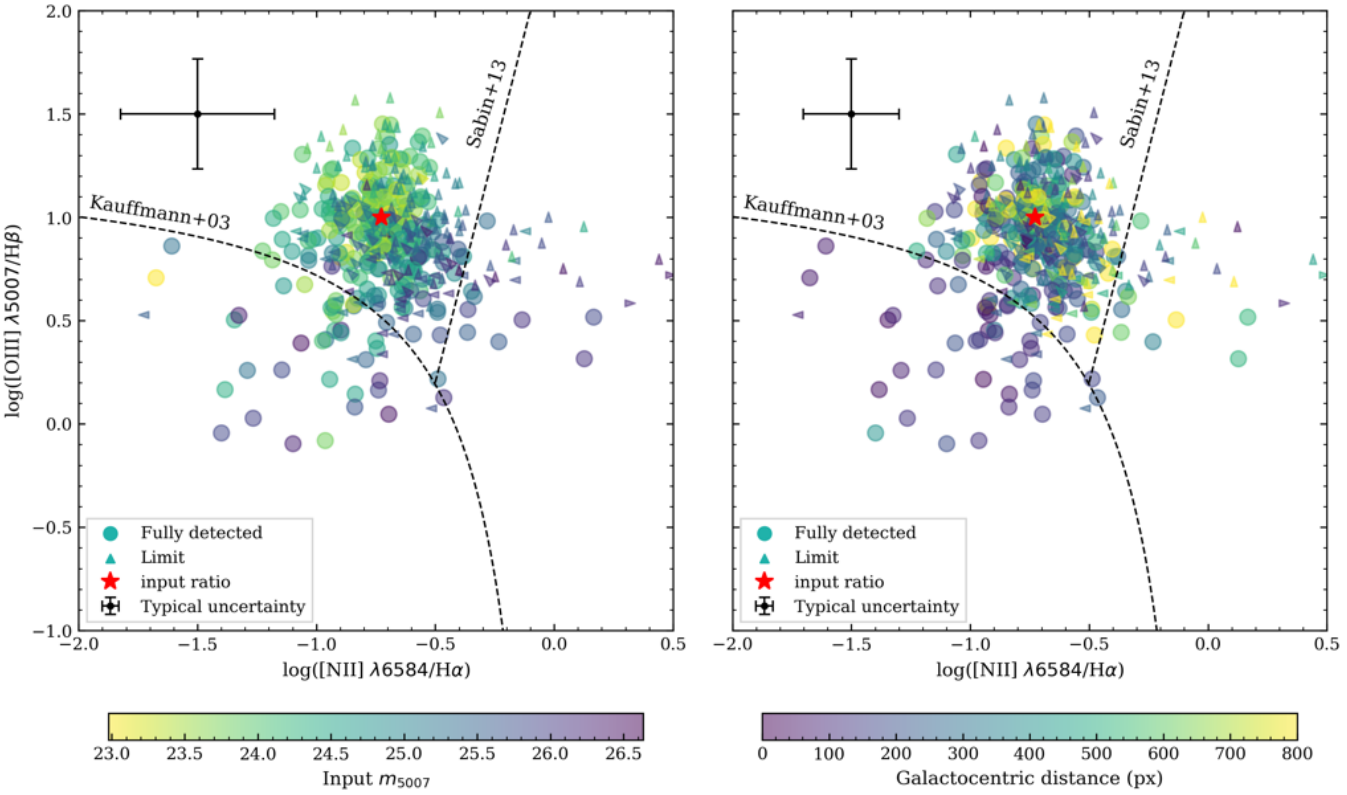

(a) NGC 4214

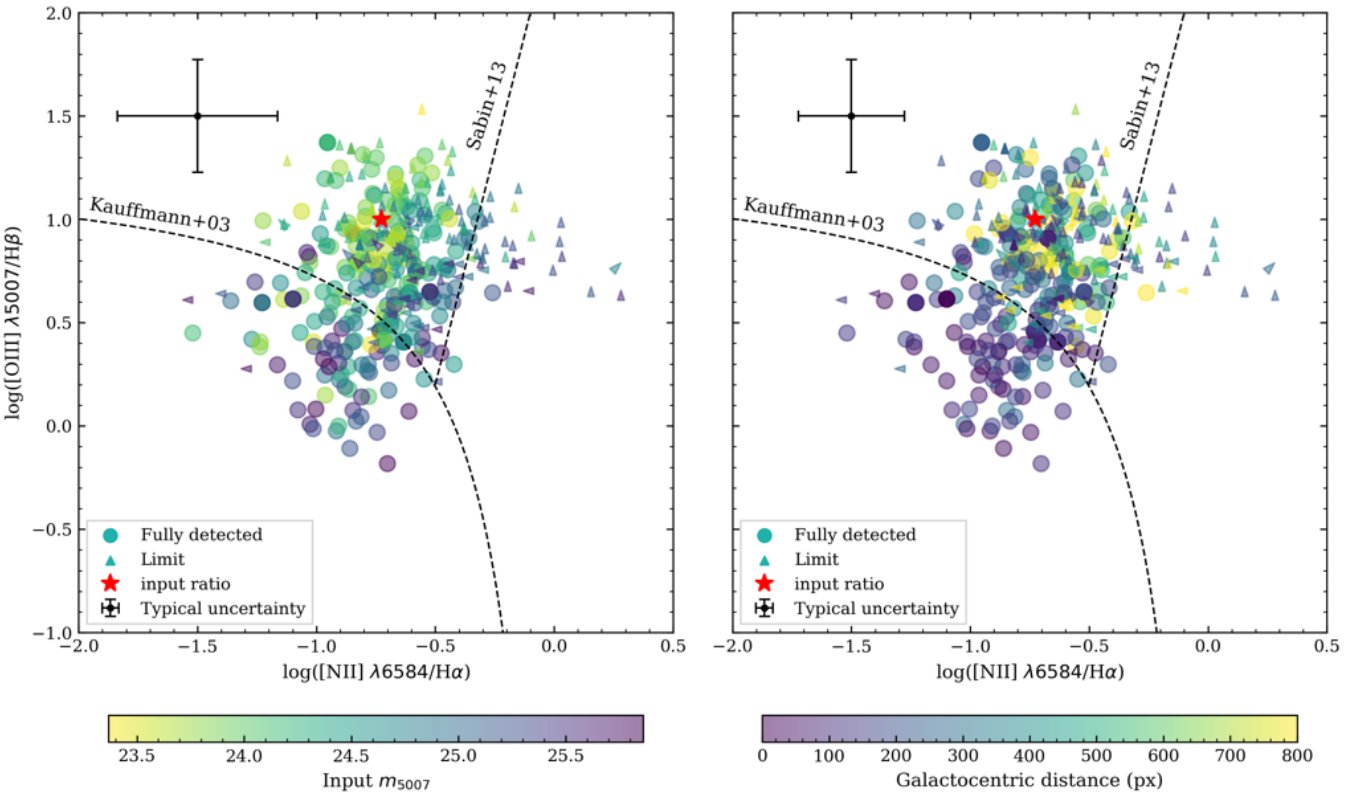

(b) NGC 4449

Figure 12. [N II]-BPT diagrams of the mock PNs generated for NGC 4214 (top) and NGC 4449 (bottom). The mock PNs are colour-coded by input apparent magnitude (left) and galactocentric distance (right). The input emission-line ratio is indicated by the star.

Downloaded from https://academic.oup.com/mnras/article/548/4/stag661/8650714 by Turun kauppakorkeakoulun kirjasto user on 10 June 2026

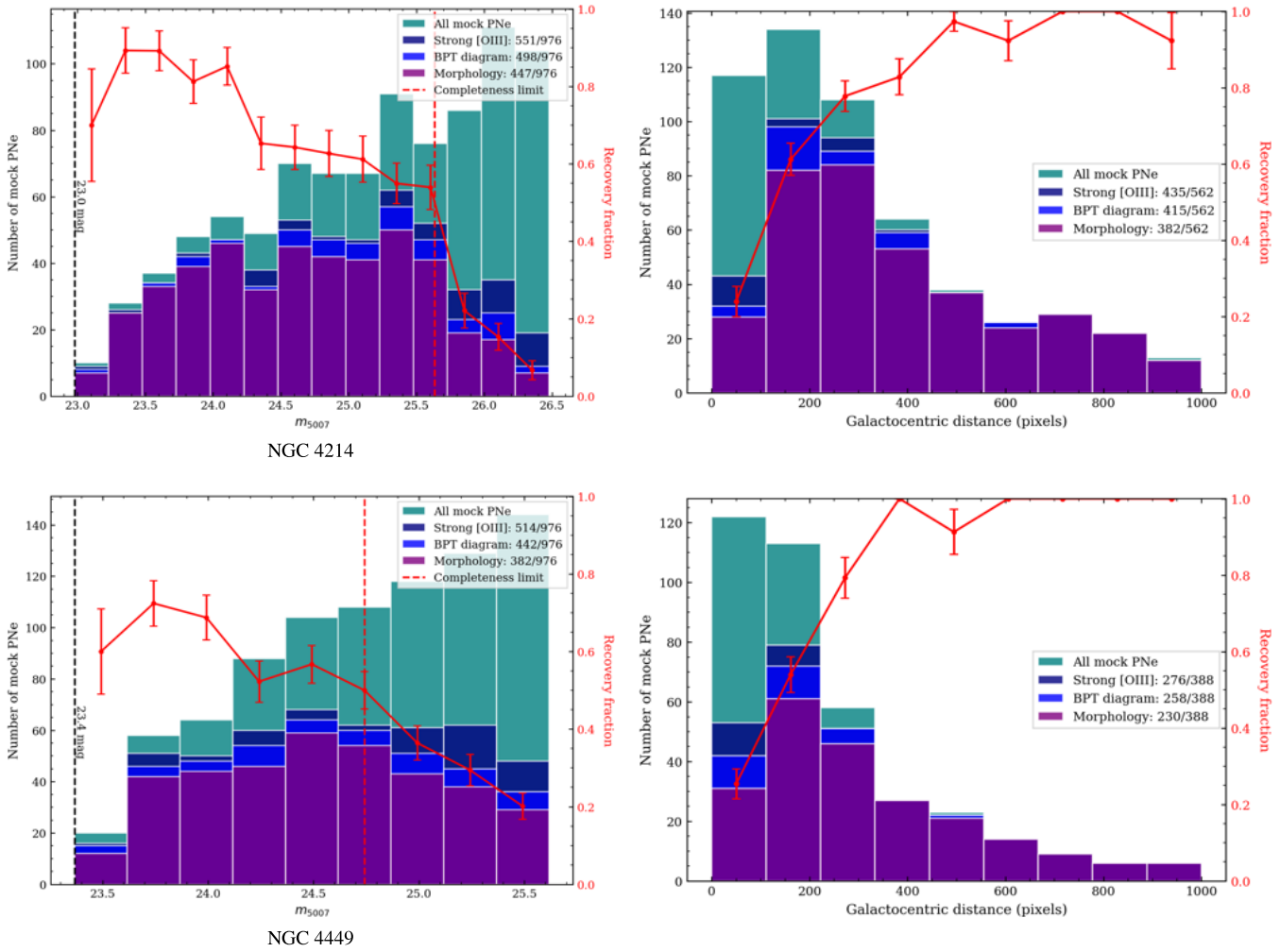

Figure 13. Recovery rates of mock PNs for NGC 4214 (top) and NGC 4449 (bottom). Left: PNLFs of the mock PNs, overlaid with the recovery fractions. Colours indicate the pipeline step at which the mock PNs fail to be recovered. From top to bottom in the legend: all generated mock PNs, recovered mock PNs with S/N([O III]) $>$ 3, recovered mock PNs which also have the correct emission-line ratios on the BPT diagram(s) and recovered mock PNs which additionally are point sources. The vertical black dashed lines indicate the bright-end cut-offs used and the vertical red dashed lines the derived completeness limits. The recovery fractions decrease toward fainter magnitudes as expected, but even the brighter bins do not have a perfect recovery due to the presence of contaminant sources. Right: mock PNs binned by galactocentric distance, overlaid with the recovery fractions, for PNs brighter than the completeness limit only. The recovery rates increase toward the galaxy outskirts, where there are fewer contaminant sources.

Overall, in addition to the 19 PNs we recover from M. A. Dopita et al. (2010) and S. Vicens-Mouret et al. (2023), we also identify six new ones. One of these, NGC4214-Y6, has a velocity in strong disagreement with those in the rest of the catalogue. We list it in our catalogue regardless, as the velocities may not be accurate, but we caution that it may be a contaminant.

A PNLF fit to the bona fide PN sample, shown in the right panel of Fig. 14, yields a distance modulus of $27.45^{+0.18}_{-0.33}$ mag and thus a distance of $3.09^{+0.25}_{-0.46}$ Mpc, where the 1σ uncertainties are as sampled from the likelihood shown in the bottom-right panel of Fig. 14. If we instead also include the possible PN sample, we get a distance modulus of $27.66^{+0.13}_{-0.26}$ mag and a distance of $3.40^{+0.20}_{-0.40}$ Mpc. Both of these distances are in agreement with the previous PNLF measurements of M. A. Dopita et al. (2010) (3.19 ± 0.36 Mpc) and S. Vicens-Mouret et al. (2023) ($3.23^{+0.18}_{-0.25}$ Mpc). We warn however that due to the nature of the PNLF, incompleteness can easily lead to an overestimation of the distance. We have plotted where our distance measurements lie compared to a more comprehensive collection of literature measurements based on different distance indicators in Fig. 15. We also list the corresponding α parameters in Table 2.

4.2 NGC 4449

In NGC 4449, we identify 606 sources with reliably detected [O III] emission. Of these, 247 (potentially) have PN-like emission-line ratios and 95 are classified as round using our automated methods. The 48 objects that are in both categories were visually inspected, leaving nine bona fide and 14 possible PNs. Even more so than for NGC4214, the majority of the contaminants which were manually removed are in the central-most area, where we cannot distinguish any point source. Some objects are round but are too large to be point sources.

The final PN catalogue of NGC 4449 is presented in Table B2, while the PN spatial distribution is shown in the left panel of Fig. 16.

Downloaded from https://academic.oup.com/mnras/article/548/4/stag661/8650714 by Turun kauppakorkeakoulun kirjasto user on 10 June 2026

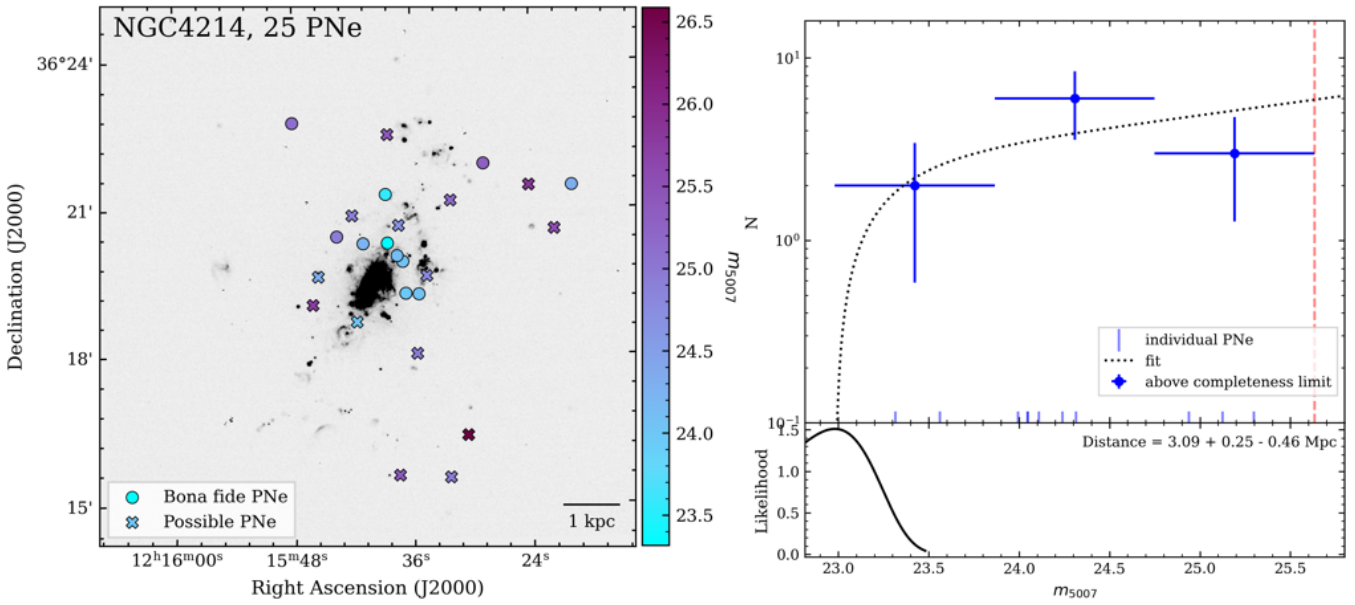

Figure 14. Left: bona fide and possible PNs of NGC 4214, overlaid on the [O III] flux map. Right: PNLF of NGC 4214, computed using only the bona fide PNs. The dotted line shows the best-fitting PNLF. The vertical dashed line indicates the completeness limit. The likelihood of the apparent bright-end cut-off is plotted underneath.

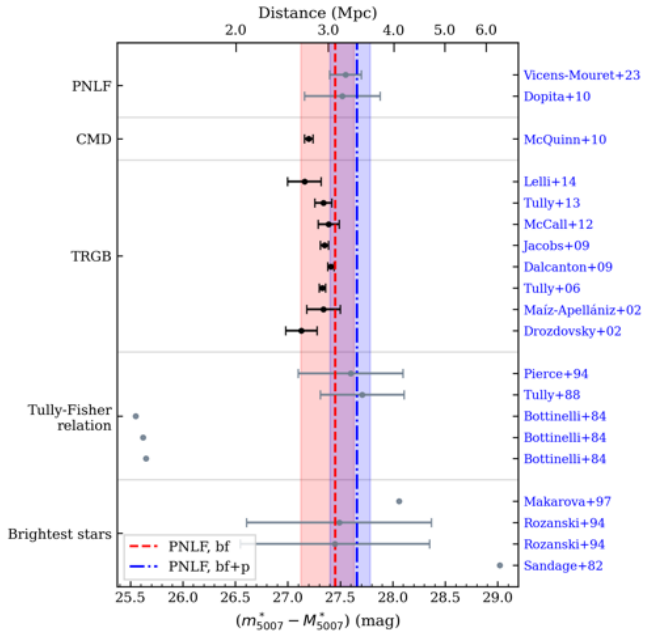

Figure 15. Comparison of our NGC 4214 PNLF distances to literature measurements. The red dashed line indicates our fit to the bona fide PNs only, the blue dot-dashed line to both bona fide and possible PNs. Shaded areas represent 1σ uncertainties. References are listed on the right, methods on the left. Distance measurements with black markers were used in calculating the assumed distance to NGC 4214, as used throughout this paper.

Using *HST* data of the central region of NGC 4449, F. Annibali et al. (2017) detected 28 PN candidates. Of these, we detect 23 with reliable [O III] emission and 10 make it into our final catalogue of bona fide and possible PNe.

From PNLF fitting to the bona fide PN sample, we derive a distance modulus of $27.96^{+0.18}_{-0.29}$ mag and thus a distance of $3.91^{+0.33}_{-0.52}$ Mpc (see the right panel of Fig. 16). Using the bona fide and possible PNs, we derive a distance modulus of $28.05^{+0.11}_{-0.19}$ mag and a distance of $4.07^{+0.21}_{-0.35}$ Mpc. Our PN sample for NGC 4449 is only complete up to 0.5 mag from the bright-end cut-off, and we only fit the PNLF to the PNs with a m_{5007} brighter than the completeness limit.

TRGB measurements have yielded distances ranging from 3.82 ± 0.27 Mpc (F. Annibali et al. 2008) to $4.30^{+0.44}_{-0.32}$ Mpc (B. A. Jacobs et al. 2009). The most recent TRGB measurement by the Legacy ExtraGalactic UV Survey (E. Sabbi et al. 2018) yields a distance of 4.01 ± 0.30 Mpc. All are consistent with our PNLF measurement. For a more comprehensive comparison of distance measurements, see Fig. 17. We list the corresponding α parameters in Table 2.

5 DISCUSSION

5.1 α parameter comparisons

We compare our $\alpha_{\rm bol,2.5}$ parameters to those of A. Buzzoni et al. (2006) in Fig. 18. We calculate $(B-V)$ using the magnitudes integrated within the infrared apertures of D. O. Cook et al. (2014). The A. Buzzoni et al. (2006) elliptical galaxies are not as blue as NGC 4214 and NGC 4449. Compared to their Local Group (LG) galaxy sample, the α parameters we derive using our bona fide samples are slightly smaller. This follows the theoretical expectation that bluer galaxies will have smaller α parameters (A. Buzzoni et al. 2006), but is in contrast to past observations which have shown the opposite trend (M. Peimbert 1990; R. Ciardullo et al. 1991, 2005; A. Buzzoni et al. 2006). However, since historically most PN surveys were carried out in ETGs, there are not much data available for relatively blue galaxies. PN catalogues for the remaining SIGNALS galaxies, which are all highly star-forming, will enable us to populate Fig. 18 further and study the correlation between α and galaxy colour.

Downloaded from https://academic.oup.com/mnras/article/548/4/stag661/8650714 by Turun kauppakorkeakoulun kirjasto user on 10 June 2026

Table 2. Number of PNs and α parameters calculated for different ranges of m_{5007} from the bright-end cut-off. The parameter $\alpha_{\rm bol}$ is calculated using the bolometric correction factor from A. Buzzoni et al. (2006). The parameter α_V is calculated using the V-band luminosity. The column headers 0.5 and 2.5 refer to the magnitude range from the best-fitting bright-end cut-off. The 'bf' sample contains only bona fide PNe, whereas the 'bf+p' sample also contains the possible PNe.

Galaxy	Sample	N		$\log(\alpha_{\rm bol})$		$\log(\alpha_V)$	
		0.5	2.5	0.5	2.5	0.5	2.5
NGC4214	bf	1.2 ± 0.5	14.8 ± 2.4	-9.16 ± 0.19	-8.07 ± 0.09	-8.85 ± 0.18	-7.75 ± 0.08
	bf+p	1.2 ± 0.5	30.5 ± 4.0	-9.16 ± 0.19	-7.75 ± 0.08	-8.85 ± 0.18	-7.44 ± 0.07
NGC4449	bf	4.3 ± 1.4	15.7 ± 3.8	-8.99 ± 0.15	-8.43 ± 0.12	-8.68 ± 0.14	-8.12 ± 0.11
	bf+p	7.2 ± 1.8	43.7 ± 7.1	-8.77 ± 0.12	-7.98 ± 0.09	-8.46 ± 0.12	-7.67 ± 0.08

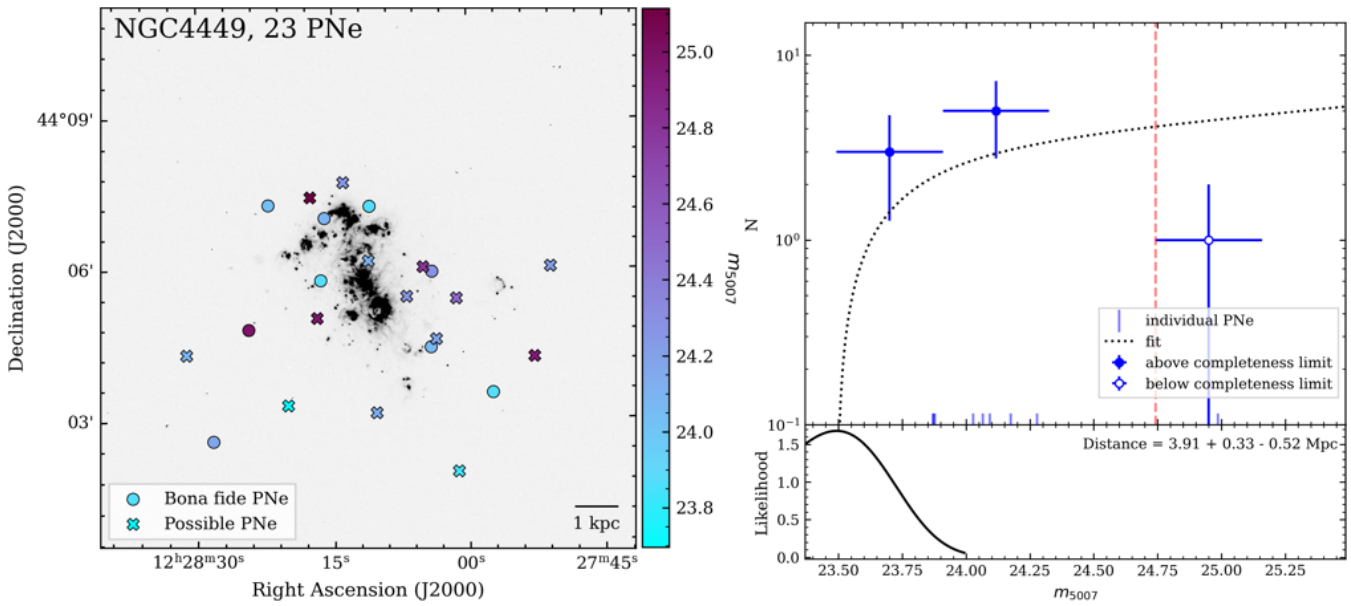

Figure 16. Same as Fig. 14 but for NGC 4449.

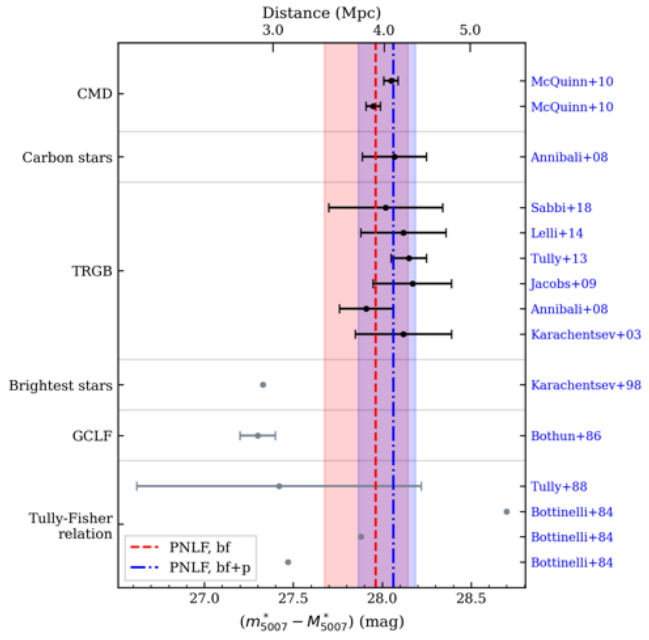

Figure 17. Same as Fig. 15 but for NGC 4449. GCLF: globular cluster luminosity function.

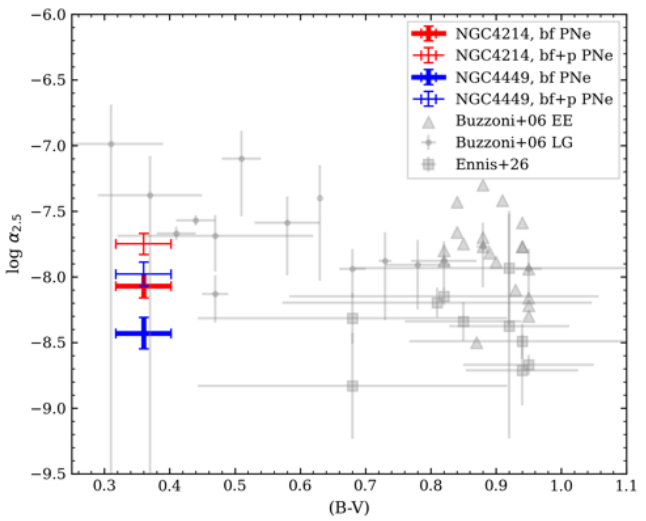

Figure 18. Comparison of the α parameters derived in this work to those of A. Buzzoni et al. (2006) and A. I. Ennis et al. (2026). The A. Buzzoni et al. (2006) elliptical galaxies and LG galaxies have been scaled using $\log(\alpha_{2.5}) = \log(\alpha_8) - 1$.

Downloaded from https://academic.oup.com/mnras/article/548/4/stag661/8650714 by Turun kauppakorkeakoulun kirjasto user on 10 June 2026

5.2 Flux and PNLF uncertainties

The PN m_{5007} listed in Tables B1 and B2 were calculated using the *HST*-derived calibration factors (Section 2.3). Additional flux uncertainties are introduced by the aperture correction, and as the correction factors were calculated using isolated undistorted objects, they may not be accurate for sources closer to the edges of the FOVs, where the PSFs are more distorted. Background subtraction is also very important for star-forming galaxies such as those from SIGNALS. There is much contaminant emission from a variety of sources (principally H II regions and SNRs), including in the [O III] line that can in turn be over- or under-subtracted. Additionally, while we do correct for foreground Milky Way extinction, we do not account for extinction within the host galaxy. All these factors can influence the derived PN apparent magnitudes, in turn impacting the derived PNLF distances.

The PNLF distances are also affected by incompleteness. Our mock PN catalogues have shown that we are unable to recover most of the PNs in the central regions of our galaxies (Fig. 13). If the brightest PNs of a galaxy remain undetected because of this, the resulting fit to the PNLF would overestimate the galaxy distance. Conversely, the presence of contaminants can lead to an underestimation of the galaxy distance, if bright compact H II regions are confused for PNs.

5.3 Velocity fitting

As discussed in Section 3.2, the fitting software ORCS requires a rather precise initial guess for the input velocity of a source. The precision required increases with increased spectral resolution. While we do not expect this to have impacted the results of this paper, it could potentially be a problem for galaxies with higher rotational velocities. The way the velocity guess in SN3 is now implemented, three different guesses are compared, and the best one is selected from the reduced χ^2. In galaxies with higher velocities, a larger number of guesses over a wider range of velocities may need to be compared.

For some noisy spectra or spectra of very faint objects, even with the aforementioned three velocity guesses, a noise peak sometimes gets fitted and an incorrect flux and velocity are returned. These bad fits can be difficult to identify, as the associated uncertainties are relatively small (S/N $\approx$ 2). We have attempted to minimize the impact on our PN catalogue by only quoting $v_{\mathrm{H}\alpha}$ for PNs which have S/N $>$ 3 in the Hα line, and using [O III] velocities otherwise (see Tables B1 and B2). For each galaxy, there are six (bona fide or possible) PNs for which this applies. One of these, NGC4214-Y6, still has an outlying $v_{[\mathrm{O\,III}]}$ (compared to the rest of the catalogue) and may therefore be a contaminant.

The required precision for fitting is only a challenge because we are looking at faint point-sources that have velocities distinct from that of the diffuse gas. For other science done using the SIGNALS data, initial velocity guesses can be easily sampled from velocity maps created using diffuse emission and H II regions.

We would like to repeat the caveat that the calibration of $v_{[\mathrm{OIII}]}$, as described in Section 3.4, relies on the assumption that the velocity offset $v_{\mathrm{SN3}} - v_{\mathrm{SN2}}$ varies smoothly across the FOV.

6 CONCLUSIONS

In this paper, we have described in detail a new automated pipeline to detect PNs in IFS data, particularly suited to the SIGNALS data obtained with SITELLE. Compared to previous methods which rely on visual inspection of [O III] flux maps or similar (e.g. S. Vicens-Mouret et al. 2023), this pipeline mostly eliminates the need for visual inspection. This speeds up the process considerably, while also making the results more objective and replicable.

We applied our new pipeline to the star-forming galaxies NGC 4214 and NGC 4449. In NGC 4214, we recovered 19 known PNs and discovered six (possible) new ones. We derived a PNLF distance of $3.09^{+0.25}_{-0.46}$ Mpc, in agreement with previous distance measurements. In NGC 4449, we confirmed 10 previously reported PNs and discovered 13 (possible) new ones. We derived a PNLF distance of $3.91^{+0.33}_{-0.52}$ Mpc, also in agreement with previous distance measurements.

As became apparent in the tests we ran using mock PNs (Fig. 13), detecting PNs superposed or close to bright star-forming regions is challenging even with the SIGNALS IFS data. This is reflected in the spatial distributions of the recovered PNs, as shown in the left panels of Figs 14 and 16. However, because the mock PN samples allow us to robustly quantify the recovery rates, we can correct for this when calculating the PN specific frequencies (α parameters). Additionally, SITELLE's wide FOV allows us to detect PNs to greater galactocentric distances, where contaminants are also less prominent. Of course, the SIGNALS data also yield the PN emission-line ratios, allowing to reject compact contaminants, and to measure velocities. It is therefore highly complementary to narrow-band *HST* PN surveys.

Although our PN detection pipeline is meant to be generic, small changes may be necessary to apply it to the other SIGNALS galaxies, to optimally handle different galaxy morphologies. For example, even though this functionality already exists in the current version of the pipeline, the initial velocity guesses required for the emission-line fits may have to be sampled from wider velocity ranges. Galaxies at larger distances may also prove more challenging, as larger fractions of the contaminants will appear spatially unresolved and only smaller (i.e. brighter) portions of the PNLFs will be probed, resulting in proportionally fewer PNs detected. This will however be partially compensated for brighter galaxies, as they inherently harbour more PNs.

Overall, the new method developed in this paper is bound to lead to hundreds of new PN discoveries in a range of star-forming galaxies, most of which have never been surveyed for PNs before.

ACKNOWLEDGEMENTS

JH and CS acknowledge the financial support from the Visitor and Mobility programme of the Finnish Centre for Astronomy with ESO (FINCA). JH also acknowledges financial support from the Turku Collegium for Science, Medicine, and Technology (TCSMT) in the form of a starting grant.

This research was based on observations obtained at the CFHT, which is operated from the summit of Mauna Kea by the National Research Council of Canada, the Institut National des Sciences de l'Univers of the Centre National de la Recherche Scientifique of France, and the University of Hawaii. The authors wish to recognize and acknowledge the very significant cultural role that the summit of Mauna Kea has always had within the indigenous Hawaiian community. The authors are most grateful to have the opportunity to conduct observations from this mountain. The observations were obtained with SITELLE, a joint project between Université Laval, ABB-Bomem, Université de Montréal, and the CFHT, with funding support from the Canada Foundation for Innovation (CFI), the National Sciences and Engineering Research

Downloaded from https://academic.oup.com/mnras/article/548/4/stag661/8650714 by Turun kauppakorkeakoulun kirjasto user on 10 June 2026

Council of Canada (NSERC), Fonds de Recherche du Québec – Nature et Technologies (FRQNT), and CFHT.

The collaboration is grateful to the FRQNT, CFHT, the Canada Research Chair programme, the National Science Foundation NSF – 2109124, Natural Sciences and Engineering Research Council of Canada NSERC – RGPIN-2023-03487, the Swedish Research Council, the Swedish National Space Board, the Royal Society, and the Newton Fund via the award of a Royal Society-Newton Advanced Fellowship (NAF\R1\180403), FAPESC, CNPq, FAPESP (2014/11156-4), FAPESB (7916/2015), and CONACyT (CB2015-254132).

This research used the facilities of the Canadian Astronomy Data Centre operated by the National Research Council of Canada with the support of the Canadian Space Agency.

This research makes use of observations made with the NASA/ESA Hubble Space Telescope obtained from the Space Telescope Science Institute, which is operated by the Association of Universities for Research in Astronomy, Inc., under NASA contract NAS 5–26555.

DATA AVAILABILITY

The data used in this work are publicly available, along with all other SIGNALS data.

REFERENCES

Annibali F., Aloisi A., Mack J., Tosi M., van der Marel R. P., Angeretti L., Leitherer C., Sirianni M., 2008, AJ, 135, 1900
Annibali F. et al., 2017, ApJ, 843, 20
Arnaboldi M., Freeman K. C., Gerhard O., Matthias M., Kudritzki R. P., Méndez R. H., Capaccioli M., Ford H., 1998, ApJ, 507, 759
Baldwin J. A., Phillips M. M., Terlevich R., 1981, PASP, 93, 5
Bhattacharya S., Arnaboldi M., Hartke J., Gerhard O., Comte V., McConnachie A., Caldwell N., 2019, A&A, 624, A132
Bhattacharya S., Arnaboldi M., Hammer F., Yang Y., Gerhard O., Caldwell N., Freeman K. C., 2023, MNRAS, 522, 6010
Bothun G. D., 1986, AJ, 91, 507
Bottinelli L., Gouguenheim L., Paturel G., de Vaucouleurs G., 1984, A&AS, 56, 381
Bradley L. et al., 2022, astropy/photutils: 1.5.0, Zenodo, Version 1.5.0,
Buzzoni A., Arnaboldi M., Corradi R. L. M., 2006, MNRAS, 368, 877
Ciardullo R., 2010, PASA, 27, 149
Ciardullo R., 2012, Ap&SS, 341, 151
Ciardullo R., Jacoby G. H., Ford H. C., Neill J. D., 1989, ApJ, 339, 53
Ciardullo R., Jacoby G. H., Harris W. E., 1991, ApJ, 383, 487
Ciardullo R., Sigurdsson S., Feldmeier J. J., Jacoby G. H., 2005, ApJ, 629, 499
Coccato L. et al., 2009, MNRAS, 394, 1249
Congiu E. et al., 2025 A&A, 700, A125
Cook D. O. et al., 2014, MNRAS, 445, 881
Cortesi A. et al., 2013, MNRAS, 432, 1010
Dalcanton J. J. et al., 2009, ApJS, 183, 67
Dopita M. A., Jacoby G. H., Vassiliadis E., 1992, ApJ, 389, 27
Dopita M. A. et al., 2010, Ap&SS, 330, 123
Douglas N. G. et al., 2002, PASP, 114, 1234
Drissen L. et al., 2019, MNRAS, 485, 3930
Drozdovsky I. O., Schulte-Ladbeck R. E., Hopp U., Greggio L., Crone M. M., 2002, AJ, 124, 811
Ennis A. I., Hartke J., Bian F., Pulsoni C., Spiniello C., Arnaboldi M., de Propris R., 2026, MNRAS, 545, staf2036
Fitzpatrick E. L., 1999, PASP, 111, 63
Flagey N., McLeod A. F., Aguilar L., Prunet S., 2020, A&A, 635, A111
Frew D. J., Parker Q. A., 2010, Publ. Astron. Soc. Aust., 27, 129
Gaia Collaboration, 2023, A&A, 674, A1
Gerhard O., Arnaboldi M., Freeman K. C., Kashikawa N., Okamura S., Yasuda N., 2005, ApJ, 621, L93
Hartke J., 2025, Front. Astron. Space Sci., 12, 1673373
Hartke J., Arnaboldi M., Longobardi A., Gerhard O., Freeman K. C., Okamura S., Nakata F., 2017, A&A, 603, A104
Hartke J. et al., 2020, A&A, 642, A46
Howell S. B., 1989, PASP, 101, 616
Hui X., Ford H. C., Ciardullo R., Jacoby G. H., 1993, ApJ, 414, 463
Jacobs B. A., Rizzi L., Tully R. B., Shaya E. J., Makarov D. I., Makarova L., 2009, AJ, 138, 332
Jacoby G. H., 1989, ApJ, 339, 39
Jacoby G. H., Ciardullo R., Roth M. M., Arnaboldi M., Weilbacher P. M., 2024, ApJS, 271, 40
Karachentsev I. D., Drozdovsky I. O., 1998, A&AS, 131, 1
Karachentsev I. D. et al., 2003, A&A, 398, 467
Kauffmann G. et al., 2003, MNRAS, 346, 1055
Kewley L. J., Dopita M. A., Sutherland R. S., Heisler C. A., Trevena J., 2001, ApJ, 556, 121
Kreckel K., Groves B., Bigiel F., Blanc G., Kruijssen J. M. D., Hughes A., Schruba A., Schinnerer E., 2017, ApJ, 834, 174
Kwok S., Purton C. R., Fitzgerald P. M., 1978, ApJL, 219, L125
Lelli F., Verheijen M., Fraternali F., 2014, A&A, 566, A71
Longobardi A., Arnaboldi M., Gerhard O., Coccato L., Okamura S., Freeman K. C., 2013, A&A, 558, A42
Maíz-Apellániz J., Cieza L., MacKenty J. W., 2002, AJ, 123, 1307
Makarova L. N., Karachentsev I. D., Georgiev T. B., 1997, Astron. Lett., 23, 378
Marigo P., Girardi L., Weiss A., Groenewegen M. A. T., Chiosi C., 2004, A&A, 423, 995
Martin T., Drissen L., Joncas G., 2015, in Taylor A. R., Rosolowsky E., eds, ASP Conf. Ser. Vol. 495, Astronomical Data Analysis Software an Systems XXIV (ADASS XXIV). Astron. Soc. Pac., San Francisco, p. 327
Martin T., Drissen L., Prunet S., 2021, MNRAS, 505, 5514
Martin T. B., Prunet S., Drissen L., 2016, MNRAS, 463, 4223
Martin T. B., Drissen L., Melchior A.-L., 2018, MNRAS, 473, 4130
McCall M. L., Vaduvescu O., Pozo Nunez F., Barr Dominguez A., Fingerhut R., Unda-Sanzana E., Li B., Albrecht M., 2012, A&A, 540, A49
McQuinn K. B. W. et al., 2010, ApJ, 721, 297
Peimbert M., 1990, Rev. Mex. Astron. Astrofis., 20, 119
Peimbert M., Torres-Peimbert S., 1983, Flower D. R., Proc. IAU Symp. 103, Planetary Nebulae Cambridge Univ. Press, Cambridge, 233
Pierce M. J., 1994, ApJ, 430, 53
Pilyugin L. S., Grebel E. K., Zinchenko I. A., 2015, MNRAS, 450, 3254
Prunet S., Rousseau-Nepton L., Baril M., 2019, Technical Report, Upgrade on SITELLE, https://www.cfht.hawaii.edu/en/news/SITELLEUpgrade/. CFHT, https://www.cfht.hawaii.edu/en/news/SITELLEUpgrade/ (Accessed Apr 2026)
Pulsoni C. et al., 2018, A&A, 618, A94
Pulsoni C., Gerhard O., Fall S. M., Arnaboldi M., Ennis A. I., Hartke J., Coccato L., Napolitano N. R., 2023, A&A, 674, A96
Roth M. M., Jacoby G. H., Ciardullo R., Soemitro A. A., Weilbacher P. M., Arnaboldi M., 2025, in De Marco O., Zijlstra A., Szczerba R., eds, Proc. IAU Symp. 384, Planetary Nebulae: A Universal Toolbox in the Era of Precision Astrophysics. Cambridge Univ. Press,, Cambridge, p. 50
Rousseau-Nepton L. et al., 2019, MNRAS, 489, 5530
Rozanski R., Rowan-Robinson M., 1994, MNRAS, 271, 530
Sabbi E. et al., 2018, ApJS, 235, 23
Sabin L. et al., 2013, MNRAS, 431, 279
Sacchi E. et al., 2018, ApJ, 857, 63
Sandage A., Tammann G. A., 1982, ApJ, 256, 339
Sarzi M., Mamon G. A., Cappellari M., Emsellem E., Bacon R., Davies R. L., de Zeeuw P. T., 2011, Monthly Notices of the RAS, 415, 2832
Scheuermann F. et al., 2022, MNRAS, 511, 6087
Schlegel D. J., Finkbeiner D. P., Davis M., 1998, ApJ, 500, 525
Soemitro A. A., Roth M. M., Weilbacher P. M., Ciardullo R., Jacoby G. H., Monreal-Ibero A., Castro N., Micheva G., 2023, A&A, 671, A142

Downloaded from https://academic.oup.com/mnras/article/548/4/stag661/8650714 by Turun kauppakorkeakoulun kirjasto user on 10 June 2026

Spiniello C. et al., 2018, MNRAS, 477, 1880
Stetson P. B., 1987, PASP, 99, 191
Torres-Peimbert S., Peimbert M., 1997, in Habing H. J., Lamers H. J. G. L. M., eds, Proc. IAU Symp. 180, Planetary Nebulae. Springer, Dordrecht, p. 175
Tully R. B., Fisher J. R., 1988, Catalog of Nearby Galaxies. Cambridge Univ. Press, Cambridge
Tully R. B. et al., 2006, AJ, 132, 729
Tully R. B. et al., 2013, AJ, 146, 86
Valenzuela L. M., Miller Bertolami M. M., Remus R.-S., Méndez R. H., 2025 A&A 699 A317
Vicens-Mouret S., Drissen L., Robert C., Rousseau-Nepton L., Martin R. P., Amram P., 2023, MNRAS, 524, 3623
Virtanen P. et al., 2020, Nat. Methods, 17, 261
Williams B. F., Dalcanton J. J., Gilbert K. M., Seth A. C., Weisz D. R., Skillman E. D., Dolphin A. E., 2011, ApJ, 735, 22

SUPPORTING INFORMATION

Supplementary data are available at *MNRAS* online.

NGC4214_PN_catalog_for_supl_table.txt

NGC4449_PN_catalog_for_supl_table.txt

Please note: Oxford University Press is not responsible for the content or functionality of any supporting materials supplied by the authors. Any queries (other than missing material) should be directed to the corresponding author for the article.

APPENDIX A: DECISION TREE FOR BPT-DIAGRAMS

Fig. A1 shows the decision tree used to determine which BPT diagrams should be considered for any given source, depending on its combination of detected and undetected emission lines.

APPENDIX B: PN TABLES

Tables B1 and B2 are our full PN catalogues, for both bona fide and possible PNs. $v_{\mathrm{H}\alpha}$ is given only for PNe with S/N $>$ 3 in the H α line; we quote $v_{[\mathrm{O\,III}]}$ otherwise.

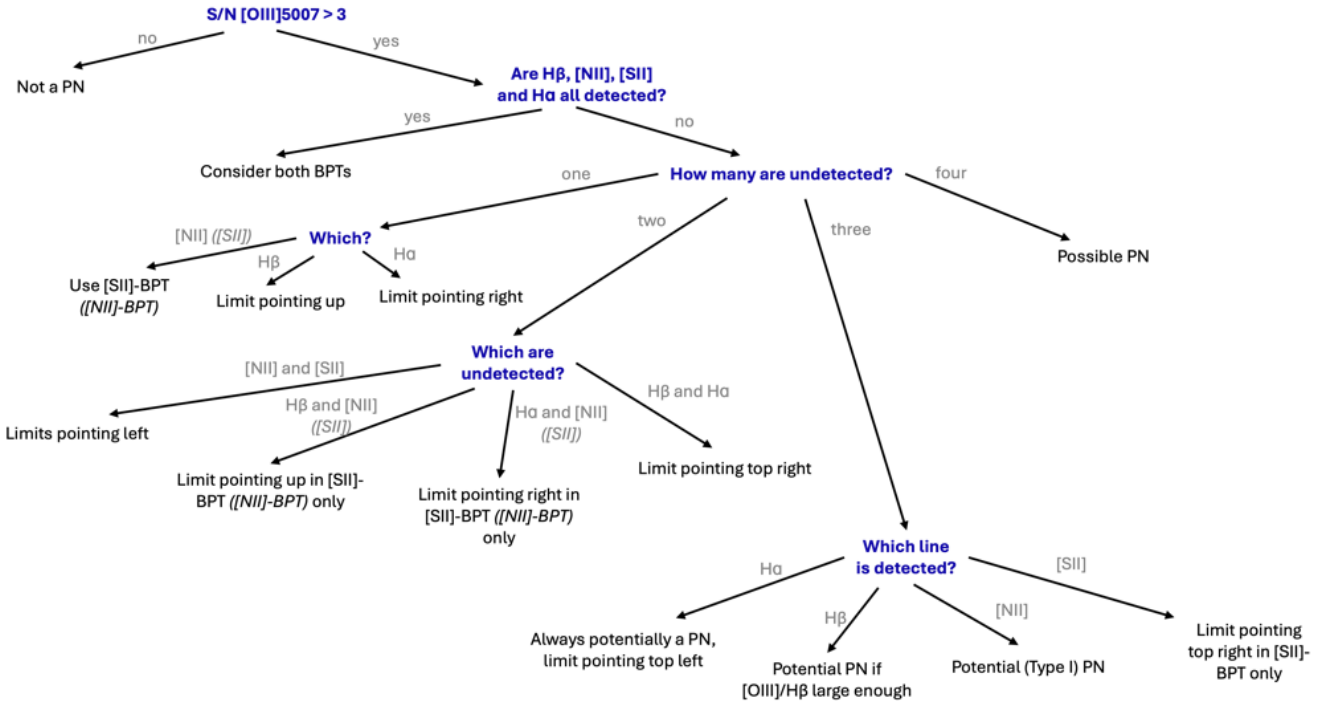

Figure A1. Decision tree showing what combination of diagnostic diagram and limits are used to classify a source as a PN candidate or contaminant. Unless stated otherwise, both the [N II]-BPT and the [S II]-BPT diagram are considered. 'Limit pointing up' would refer to a lower limit on the [O III]/H βemission line ratio.

Downloaded from https://academic.oup.com/mnras/article/548/4/stag661/8650714 by Turun kauppakorkeakoulun kirjasto user on 10 June 2026

Table B1. PN catalogue of NGC 4214.

ID	RA (J2000) (hh:mm:ss)	Dec (J2000) (deg:arcmin:arcsec)	m_{5007} (mag)	$v_{H\alpha}$ (km s^{-1})	$v_{[O\,III]}$ (km s^{-1})	$F([O\,III])$	$F(H\,\beta)$	$F(H\,\alpha)$	$F([N\,II])$	$F([S\,II])$	[N II]-BPT	[S II]-BPT	Final
						(10^{-17} erg s^{-1} cm^{-2})							
(1)	(2)	(3)	(4)	(5)	(6)	(7)	(8)	(9)	(10)	(11)	(12)	(13)	
VDR2	12:15:19.609	36:21:27.84	24.3 ± 0.1		280 ± 10	60 ± 8	5 ± 3	22 ± 5	4 ± 3	<4	l		b.f.
VDR3	12:15:21.403	36:20:34.12	25.5 ± 0.2		220 ± 10	20 ± 4	5 ± 3	11 ± 2	4 ± 2	<3	p		p
VDR5	12:15:23.947	36:21:28.42	25.8 ± 0.2	300 ± 20		15 ± 3	5 ± 2	6 ± 3	9 ± 4	<4	p		p
VDR6	12:15:31.960	36:21:10.42	25.2 ± 0.2		260 ± 10	28 ± 5	5 ± 2	12 ± 4	7 ± 3	<4	p		p
VDR7	12:15:32.297	36:15:27.82	24.9 ± 0.2		260 ± 20	34 ± 6	8 ± 4	20 ± 6	<4	<5	p	p	p
VDR8	12:15:35.551	36:18:00.19	25.0 ± 0.2		270 ± 10	33 ± 5	8 ± 3	17 ± 4	5 ± 3	<4	p		p
VDR9	12:15:37.487	36:15:30.52	25.4 ± 0.2	240 ± 20		22 ± 5	7 ± 3	11 ± 5	3 ± 3	<4	p		p
VDR11	12:15:38.629	36:21:18.35	23.6 ± 0.1		271 ± 7	120 ± 10	7 ± 3	33 ± 5	4 ± 2	<4	l		b.f.
VDR12	12:15:42.108	36:20:52.23	24.9 ± 0.2	230 ± 20		36 ± 6	<3	4 ± 2	<2	<4	p	p	p
VDR13	12:15:43.710	36:20:26.07	24.9 ± 0.2		330 ± 20	34 ± 6	<3	10 ± 3	<2	<3	l	l	b.f.
VDR15	12:15:48.130	36:22:47.15	25.1 ± 0.2		326 ± 9	28 ± 5	7 ± 3	20 ± 3	5 ± 2	4 ± 3	l	p	b.f.
D1	12:15:34.473	36:19:36.88	24.8 ± 0.2	330 ± 20		40 ± 6	<3	8 ± 4	<4	<6	p	p	p
D3	12:15:35.310	36:19:14.17	24.0 ± 0.1	280 ± 10		77 ± 10	6 ± 3	11 ± 4	<3	<4	l	l	b.f.
D4	12:15:36.656	36:19:15.05	24.0 ± 0.1		307 ± 9	80 ± 10	8 ± 4	28 ± 5	6 ± 3	8 ± 5	l	l	b.f.
D5	12:15:36.925	36:19:54.82	24.0 ± 0.1		240 ± 20	80 ± 10	<5	26 ± 8	9 ± 6	12 ± 8	l	l	b.f.
D6	12:15:37.510	36:20:02.05	24.1 ± 0.2		310 ± 10	70 ± 10	<6	47 ± 10	7 ± 5	9 ± 8	l	l	b.f.
D7	12:15:38.489	36:20:17.83	23.3 ± 0.1		304 ± 7	150 ± 20	6 ± 4	60 ± 9	4 ± 4	<5	l		b.f.
D14	12:15:41.002	36:20:17.26	24.2 ± 0.1		291 ± 9	64 ± 8	4 ± 4	29 ± 5	<3	7 ± 4		l	b.f.
D17	12:15:46.246	36:19:01.22	25.7 ± 0.2		270 ± 20	16 ± 3	3 ± 3	14 ± 4	<2	<4	p	p	p
Y1	12:15:41.716	36:18:39.97	24.0 ± 0.1		292 ± 6	79 ± 10	24 ± 4	55 ± 7	<3	17 ± 5		p	p
Y2	12:15:45.665	36:19:36.31	24.3 ± 0.1		325 ± 6	60 ± 8	18 ± 4	63 ± 8	<3	18 ± 4		p	p
Y3	12:15:37.327	36:20:39.80	24.6 ± 0.2		315 ± 7	44 ± 7	16 ± 4	45 ± 7	<3	14 ± 5		p	p
Y4	12:15:28.564	36:21:55.64	25.3 ± 0.2		264 ± 6	24 ± 4	8 ± 2	53 ± 7	3 ± 3	16 ± 4	c	l	b.f.
Y5	12:15:38.372	36:22:32.39	25.4 ± 0.2		300 ± 10	22 ± 4	10 ± 3	28 ± 6	5 ± 3	14 ± 5	p	p	p
Y6	12:15:30.469	36:16:19.29	26.6 ± 0.3	30 ± 40		7 ± 2	<2	4 ± 2	3 ± 2	<3	p		p

Note. Flux upper limits are listed for non-detections. 1σ uncertainties are quoted to 1 significant figure. Columns: (1) PN ID. (2)–(3) Coordinates in the FK5 reference frame. (4) [O III]λ5007 apparent magnitude. (5)–(6) Velocity as measured from $v_{H\alpha}$ or $v_{[O\,III]}$, respectively. (7)–(11) Emission-line flux. (12) Likely (l) or possible (p) classification based on the [N II]-BPT only. (13) Likely (l) or possible (p) classification based on the [S II]-BPT only. (14) Final classification of bone fide (b.f.) and possible (p) PNs. A machine readable version of this table has been provided in the online supplementary material.

Downloaded from https://academic.oup.com/mnras/article/548/4/stag661/8650714 by Turun kaupunkikeskoulun kirjasto user on 10 June 2026

Table B2. PN catalogue of NGC 4449.

ID	RA (J2000) (hh:mm:ss)	Dec (J2000) (deg:arcmin:arcsec)	m_{5007} (mag)	$v_{H\alpha}$ (km s^{-1})	$v_{[O\,III]}$ (km s^{-1})	$F([O\,III])$	$F(H\,\beta)$	$F(H\,\alpha)$	$F([N\,II])$	$F([S\,II])$	[N II]-BPT	[S II]-BPT	Final
						(10^{-17} erg s^{-1} cm^{-2})							
(1)	(2)	(3)	(4)	(5)	(6)	(7)	(8)	(9)	(10)	(11)	(12)	(13)	
A1	12:28:04.145	44:04:24.70	24.1 ± 0.3		229 ± 6	80 ± 20	7 ± 5	19 ± 5	<3	<4	l	l	b.f.
A2	12:28:03.541	44:04:34.45	24.2 ± 0.3	200 ± 10		70 ± 20	15 ± 6	30 ± 10	<5	<8	p	p	p
A3	12:28:03.984	44:05:56.47	24.3 ± 0.3		183 ± 5	60 ± 20	<5	22 ± 6	7 ± 3	<4	l		b.f.
A5	12:28:13.962	44:07:44.75	24.2 ± 0.3		197 ± 5	60 ± 20	8 ± 4	19 ± 5	<3	6 ± 5		p	p
A10	12:28:16.995	44:05:00.13	25.0 ± 0.3	310 ± 20		33 ± 10	<4	11 ± 4	<3	<4	p	p	p
A12	12:28:01.244	44:05:23.80	24.5 ± 0.3	240 ± 10		50 ± 10	8 ± 4	16 ± 7	<4	<6	p	p	p
A14	12:28:06.851	44:05:26.26	24.3 ± 0.3	250 ± 20		60 ± 20	<7	15 ± 9	<5	9 ± 9		p	p
A16	12:28:16.566	44:05:45.87	23.9 ± 0.3		179 ± 5	90 ± 20	32 ± 10	80 ± 20	25 ± 8	17 ± 9	l	p	b.f.
A24	12:28:11.166	44:06:09.62	24.1 ± 0.3	140 ± 30		70 ± 20	<9	18 ± 7	<6	<9	p	p	p
A28	12:28:16.112	44:07:01.45	24.1 ± 0.3	200 ± 40		70 ± 20	<10	12 ± 4	<4	7 ± 5		l	b.f.
Y1	12:28:20.277	44:03:14.77	23.7 ± 0.2		209 ± 6	110 ± 20	13 ± 6	28 ± 8	<4	<5	p	p	p
Y2	12:28:01.165	44:01:55.14	23.8 ± 0.2		221 ± 4	90 ± 20	19 ± 6	70 ± 20	<4	12 ± 6		p	p
Y3	12:28:11.009	44:07:15.94	23.9 ± 0.3		216 ± 4	90 ± 20	29 ± 8	60 ± 10	16 ± 5	25 ± 6	l	l	b.f.
Y4	12:27:57.214	44:03:29.86	23.9 ± 0.2		207 ± 6	90 ± 20	5 ± 4	24 ± 7	<4	<5	l	l	b.f.
Y5	12:28:22.422	44:07:17.18	24.0 ± 0.3	210 ± 10		80 ± 20	<5	24 ± 8	<4	<6	l	l	b.f.
Y6	12:28:31.603	44:04:16.53	24.1 ± 0.3		189 ± 5	70 ± 20	13 ± 5	19 ± 5	<3	6 ± 4		p	p
Y7	12:28:10.330	44:03:05.46	24.1 ± 0.3		149 ± 6	70 ± 20	7 ± 4	21 ± 6	9 ± 4	<5	p		p
Y8	12:28:28.562	44:02:32.75	24.2 ± 0.3		201 ± 6	70 ± 20	<4	13 ± 4	6 ± 3	4 ± 4	l	l	b.f.
Y9	12:27:50.645	44:06:02.11	24.2 ± 0.3	210 ± 10		60 ± 20	<4	14 ± 5	10 ± 4	<4	p		p
Y10	12:28:04.985	44:06:02.06	24.8 ± 0.3		229 ± 6	40 ± 10	8 ± 5	16 ± 5	<3	<5	p	p	p
Y11	12:27:52.526	44:04:13.11	24.9 ± 0.3	250 ± 20		34 ± 8	6 ± 4	10 ± 3	<3	<4	p	p	p
Y12	12:28:24.700	44:04:46.42	25.0 ± 0.3	160 ± 20		32 ± 8	<3	15 ± 6	<4	6 ± 6		l	b.f.
Y13	12:28:17.701	44:07:26.59	25.1 ± 0.3		199 ± 5	29 ± 8	7 ± 4	18 ± 5	<3	11 ± 4		p	p

Note. Flux upper limits are listed for non-detections. 1σ uncertainties are quoted to 1 significant figure. Columns: (1) PN ID. (2)–(3) Coordinates in the FK5 reference frame. (4) [O III]λ5007 apparent magnitude. (5)–(6) Velocity as measured from $v_{H\,\alpha}$ or $v_{[O\,iii]}$, respectively. (7)–(11) Emission-line flux. (12) Likely (l) or possible (p) classification based on the [N II]-BPT only. (13) Likely (l) or possible (p) classification based on the [S II]-BPT only. (14) Final classification of bone fide (b.f.) and possible (p) PNs. A machine readable version of this table has been provided in the online supplementary material.

This paper has been typeset from a TEX/LATEX file prepared by the author.

© The Author(s) 2026.
Published by Oxford University Press on behalf of Royal Astronomical Society. This is an Open Access article distributed under the terms of the Creative Commons Attribution License (https://creativecommons.org/licenses/by/4.0/), which permits unrestricted reuse, distribution, and reproduction in any medium, provided the original work is properly cited.

Downloaded from https://academic.oup.com/mnras/article/548/4/stag661/8650714 by Turun kauppakorkeakoulun kirjasto user on 10 June 2026